



UWL REPOSITORY

repository.uwl.ac.uk

Performance analysis and design implementation of a novel polymer hollow fiber liquid desiccant dehumidifier with aqueous potassium formate

Chen, Xiangjie, Zhang, Nan, Su, Yuehong, Aydin, Devrim, Zheng, Hongfei, Bai, Hongyu, Georgakis, Apostolos, Jarimi, Hasila and Riffat, Saffa (2019) Performance analysis and design implementation of a novel polymer hollow fiber liquid desiccant dehumidifier with aqueous potassium formate. Thermal Science and Engineering Progress, 13. p. 100366.

<http://dx.doi.org/10.1016/j.tsep.2019.100366>

This is the Accepted Version of the final output.

UWL repository link: <https://repository.uwl.ac.uk/id/eprint/6331/>

Alternative formats: If you require this document in an alternative format, please contact: open.research@uwl.ac.uk

Copyright: Creative Commons: Attribution-Noncommercial-No Derivative Works 4.0

Copyright and moral rights for the publications made accessible in the public portal are retained by the authors and/or other copyright owners and it is a condition of accessing publications that users recognise and abide by the legal requirements associated with these rights.

Take down policy: If you believe that this document breaches copyright, please contact us at open.research@uwl.ac.uk providing details, and we will remove access to the work immediately and investigate your claim.

Performance analysis and design implementation of a novel polymer hollow fiber liquid desiccant dehumidifier with aqueous potassium formate

Nan Zhang¹, Xiangjie Chen^{2,3}, Yuehong Su², Devrim Aydin⁴, Hongfei Zheng^{1,*}, Hongyu Bai², Apostolos Georgakis⁵, Hasila Jarimi², Saffa Riffat²

¹School of Mechanical Engineering, Beijing Institute of Technology, Beijing 100081, China

²Department of Architecture and Built Environment, the University of Nottingham, University Park, Nottingham, NG7 2RD, UK.

³Department of Energy and Power Engineering, University of Shanghai for Science and Technology, Jungong Road No. 516, Shanghai, 200031, China

⁴Department of Mechanical Engineering, Eastern Mediterranean University, G. Magosa, TRNC Mersin 10, Turkey.

⁵School of Computing and Engineering, University of West London, W5 5RF, UK.

Contact: Xiangjie Chen; Email:xiangjie.chen@nottingham.ac.uk ; Hongfei Zheng;

Email:hongfeizh@bit.edu.cn

Abstract

A novel cross-flow liquid desiccant polymer hollow fiber dehumidifier (PHFD) is investigated numerically in this paper.

The main objective of this research is to simulate, validate the numerical model for future design implementations. The experimental verified simulation data will be used to develop a set of design and implementation tables and charts as the guidance for selecting the number of fibres and the solution-to-air mass flow ratio of the PHDF under given conditions. A numerical model is developed to simulate the performance of the proposed innovative dehumidifier. This model is validated against three sets of data, i.e, the experimental obtained testing results, analytical correlations and the modelling results from the literature. The influence of various operating conditions such as inlet air properties (i.e. velocity, relative humidity) and inlet solution properties (i.e. temperature, concentration, mass flow rate) on the dehumidification sensible, latent, and total effectiveness, moisture removal rate are numerically analyzed. Dimensionless parameters including the number of heat transfer unit (NTU) and the number of mass transfer unit (NTU_m), the solution to air mass flow rate ratio (m^*), and the air to solution specific humidity ratio (ω_r^*) have been used to evaluate the system performance. The results show that the increase in NTU and NTU_m lead to a substantial change in dehumidification effectiveness. When the NTU increases from 0.47 to 7, the sensible effectiveness rises from 0.35 to 0.95. Increasing ω_r^* is another good option for increasing the amount of the absorbed moisture without influencing the latent effectiveness. For an increase of ω_r^* from 1.4 to 2.2, the air inlet and outlet specific humidity difference varies in the range of 0.008 kg/kg and 0.018 kg/kg.

Keywords: Polymer hollow fibre dehumidifier, potassium formate solutions, heat transfer, mass transfer, numerical analysis, experimental validation, performance implementation

1. Introduction

Around 40% and 50% of the EU's total energy and electricity consumption, respectively, takes place in buildings [1]. The majority of this comes from the combustion of fossil fuels, contributing to approximate 36% of the EU's total carbon emissions [2]. By 2025, the installed air-conditioning capacity in Europe is predicted to further increase by 50%-60% compared with that in 2010 [3]. The above situation has fueled research into energy-efficient and environmentally-friendly air-conditioning systems.

Dehumidification is an inseparable part of air conditioning, both for commercial and residential cooling, and for humidity control in a wide range of industries (e.g. food, textile, wood processing, printing, and crop drying). Recent research into efficient dehumidifiers has been growingly focusing on liquid desiccant-integrated processes [4], and evaporative cooling [5, 6]. This approach introduces important advantages compared with the conventional vapour compression (VC) systems. Firstly, it does not require refrigerants such as CFCs and HFCs, which are known to be detrimental to ozone depletion and global warming. Secondly, it results in energy savings of around 30% [5] by avoiding the deep-cooling-and-reheating cycles (VC systems remove moisture from the air by cooling it below its dew point so that water vapour condenses on a cooling coil, and then reheat the dehumidified air to reach the desired temperature). Liquid desiccant-based systems dehumidify the air by utilizing the natural hygroscopic properties of desiccant materials, i.e. their ability to absorb moisture. Finally, thanks to their lower consumption, liquid desiccant dehumidifiers can easily be powered by renewable energy (e.g. solar, wind) [7-10], further reducing carbon emissions.

Central to the design of liquid desiccant dehumidifiers is the flow pattern in which the incoming humid air gets in contact with the moisture absorbing material. There are two broad types of dehumidifier designs: direct contact [11-17] and indirect contact [18-21]. Direct contact simply exposes the liquid desiccant to the flowing air. A two stage liquid desiccant dehumidifier proposed by Xiong et al. [22] showed a double fold thermal performance improvement compared with a conventional dehumidifier. A fin-tube type internally-cooled liquid desiccant dehumidifier was explored by Luo et al. using experimental analysis [23] and CFD modeling [24]. Ou et al. [25], conducted experimental and analytical studies on a combined system with a cooling coil, obtaining 22.3% of energy savings.

A disadvantage of direct contact is that the air passing over the liquid desiccant results in droplets of the desiccant migrating across the dehumidifier. To mitigate this, thin membrane plate dehumidifiers with different configurations have been studied by various researchers. A cross flow membrane contactor was analyzed by Das and Jain [26] using LiCl as the liquid desiccant. The results indicated that the reduced air channel gap within the membrane contactor lead to improved energy efficiency. Ge et al. [27-30] presented a counter-cross-flow single-plate membrane contactor with an air gap of 5mm using again LiCl as the desiccant. Their numerical and experimental results confirmed that the solution concentration and the moisture flow rate were the main factors for efficient moisture removal. Moghaddam et al. [31-34] tested an air-to-liquid membrane energy exchanger using LiCl. The results showed that the dehumidifier effectiveness (both sensible and latent) was sensitive to the concentration of the inlet solution.

Despite the extensive research on the performance of various packed beds [16, 17, 22, 25] or thin membrane plate dehumidifiers [27, 31], the liquid droplet carryover problem could not be solved. Since most liquid desiccants (LiCl , CaCl_2 and LiBr) are corrosive and harmful to health, the spreading, as well as the proper subsequent removal of their carryovers becomes a major problem. In order to address this, permeable polymer hollow fiber dehumidifiers (PHFD) have been proposed as an alternative for direct contact dehumidifiers. Due to the microscopic size of its pore (less than $100\mu\text{m}$) [35], the hollow fibre allows the moisture of the incoming air to penetrate through its porous wall, while preventing any liquid desiccant droplets from getting in contact with the processed air. Moreover, the small inside diameter (less than 0.1mm) of the polymer hollow fiber leads to significantly enhanced surface contact areas, which can be regarded as another great advantage of the PHFD. A numerical simulation model for a hollow-fiber dehumidification system was proposed by Zhang et al. [36]. They concluded that the dehumidifier's effectiveness and dimensionless parameters were influenced by the varying air flow rate. Huang et al. [37] analyzed the coupled heat and mass transfer in parallel-plate membranes by numerical analysis. Their findings showed that the boundary conditions were non-uniform both in the air side and the solution side. A CFD package-FLUENT module was set-up by Zhang et al. [38]. Their analytical data indicated that the packing ratio had a major impact on the flow distribution. The above team, has recently also worked on integrating liquid desiccant-based membranes into heat pumps [39, 40] and heat recovery systems [41].

The research work presented in this paper aims to bridge the following research gaps: (1) As summarized in Table 1, the work published in the field of hollow fiber integrated dehumidification systems has mostly focused on theoretical modelling [36-39], with hardly any experimental results. Attempts have been made to obtain the overall heat and mass transfer coefficients for a polymer hollow fiber integrated shell-and-tube heat exchanger [42]. Due to the difficulties in the manufacturing process of PHFD (especially related to potting the hollow fiber bundles), very limited effort has been made to validate the models against experimental testing results. (2) The dehumidification capacity of PHFD with aqueous potassium formate (KCOOH) as the liquid desiccant has not been adequately addressed in the literature. With its advantages of low price, low toxicity and low corrosiveness compared with other liquid desiccants [43], the aqueous potassium formate solution is a preferable, environmentally friendly liquid desiccant. The associated higher vapour pressure of KCOOH solutions means that smaller amounts of energy are required for the regeneration stage [43], leading to a great energy saving potential for the proposed PHFD. (3) Most importantly, previous modelling works presented in the literature are largely based on specific working conditions and certain PHFD module configurations, which can hardly be duplicated practically in the design of PHFD modules for arbitrarily given operating conditions. (4) The effects of different fiber numbers on the dehumidification performance of PHFD have not been investigated to date. A detailed summary of previous research work and the research gap this paper is aiming to bridge is shown in Table 1.

This paper introduces numerical and experimental investigations of a polymer hollow fiber integrated dehumidifier (PHFD) with a potassium formate solution. It starts with numerical evaluations of heat and mass transfer in such cross-flow liquid desiccant PHFDs. As opposed to thin plate membrane contactors [31-34], the developed model takes into consideration the

porous and permeable feature of the polymer hollow fibers. Firstly, the derived mathematical model was verified against three sets of data, i.e. experimental testing results, analytical results, and published simulation results. Then, the impact of various operating conditions, i.e. the inlet air properties (velocity, relative humidity), and the inlet solution properties (concentration, mass flow rate, temperature) on: (a) the dehumidification effectiveness (sensible, latent, and total), (b) the moisture removal rate, and (c) the outlet parameters (air temperature and specific humidity), were numerically calculated and analyzed using the verified model. Dimensionless parameters including the number of heat transfer unit (NTU) and number of mass transfer unit (NTU_m), the solution-to-air mass flow ratio (m^*), the air-to-solution specific humidity ratio (ω_r^*) have been employed to evaluate the dehumidification performance of the proposed PHFD. Finally, the effects of fiber number on the dehumidification performance have been analyzed. Based on the numerical modelling, a set of PHFD performance tables and charts have been developed and verified against experimental results [44]. These can serve as a guidance for the selection of appropriate number of fibres and the solution-to-air mass flow ratio of the PHDFs under given conditions. With no iterative calculation required, this would give the designers great convenience. The outcomes in the form of tables and charts can be used in the design of aqueous KCOOH based PHFD. The research approach in this paper can also be adopted for other types of liquid desiccants and PHFD configurations.

Table 1 Summary of the existing works and the research gap bridged by the present research

Reference	Dehumidifier type	Flow patter	Direct/indirect contact between air and liquid desiccant	Numerical/ Experimental investigation	Desiccant solution	Research methodology and conclusion
Peng and Zhang [7]	Packed bed	Parallel flow	Direct	Numerical	LiCl	The analytical results were proved to agree well with modelling data.
Li et al. [8]	Packed bed	Parallel flow	Direct	Both	LiCl	The proposed simplified model agreed well with the experimental data.
Xiao et al. [9]	Packed bed	Counter flow	Direct	Numerical	LiCl	The proposed outdoor air liquid desiccant system could be adopted for humid and hot climates, with the system performance improvement of 19.9-38.4%.
Wang et al. [16]	Packed bed	Parallel flow	Direct	Both	LiCl	The work conducted was mainly focused on the input and output data for system control and optimization, therefore no iterative process was involved.
Wu et al. [17]	Packed bed	Counter flow	Direct	Numerical	LiCl	The control strategy applied in this work avoids the continuous solution exchange, which allowed a series of dehumidifiers to work together for large scale building applications.

Xiong et al. [22]	Packed bed	Counter flow	Direct	Numerical	CaCl ₂	The two-stage dehumidification system was shown to offer significant performance improvement, with thermal COP of 0.73 and exergy efficiency of 23%.
Luo et al. [23, 24]	Fin tube heat exchanger	Counter flow	Indirect	Both	LiCl	The proposed fin type dehumidifier was made of light weight, corrosion resistant metal, which proved to offer dehumidification efficiency above 60%.
Moghaddam et al. [31]	Thin plate membrane energy exchanger	Counter-cross flow	Indirect	Both	LiCl	Made from semi-permeable membrane panels, the dehumidifier was designed with 2.4mm solution channel sandwiched between two solution panels.
Zhang et al. [36] and Huang et al. [37]	Polymer hollow fiber membrane contactor	Cross flow	Indirect	Numerical	LiCl	A free surface model with defined boundary conditions was developed to evaluate hollow fiber membrane module. However, the experimental results were not available.
Zhang et al. [39, 40]	Two stage hollow fiber membrane contactor	Counter flow	Indirect	Numerical	LiCl	A heat pump powered two-stage dehumidification system using membrane as the dehumidifier was numerically analyzed with performance improvement of 20% against single stage system. However, the model was not validated against experimental results.
The present work	Polymer hollow fiber integrated dehumidifier (PHFD)	Cross flow	Indirect	Both	KCOOH (Potassium formate)	Model validation have been carried out in three parts: validation against 1) laboratory obtained testing results, 2) previous established analytical results and 3) other published simulation results from the literature. Based on this, a set of PHFD performance tables and charts have been developed, which will be easily applied by designers in the practical cases.

148 2. The mathematical model

149 2.1 Heat/mass transfer coefficients for air side and solution side

150 As shown in Fig. 1, the PHFD module is designed as the interface between air flow and
151 solution flow, which respectively occur outside and inside of the hollow fibers. The heat
152 and mass transfer process of the PHFD model can be considered as three mechanisms: the
153 sensible and latent heat transfer between the air side and the solution side, and the moisture
154 transfer from the air side into the solution side. Therefore, the heat and mass transfer
155 coefficients for both the air side and solution side can be calculated using the modified

Gnielinski correlation [45, 46] and the Leveque equation [47, 48], as described in the following sections.

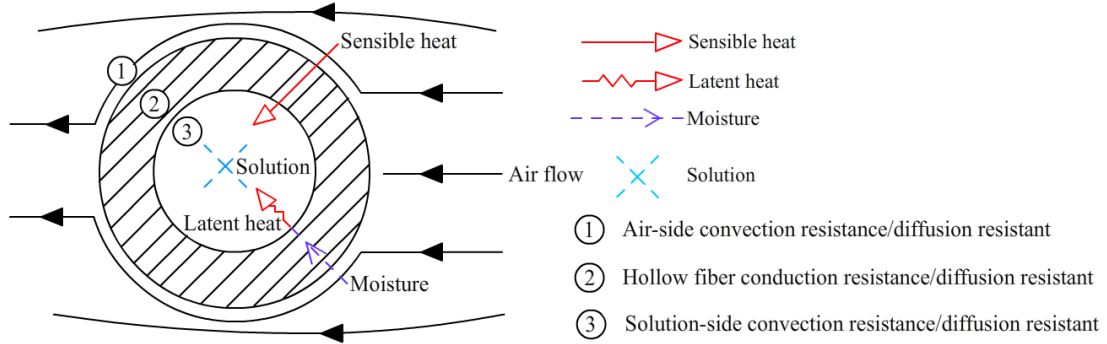


Fig. 1 Heat and mass transfer scheme of the PHFD model

2.1.1 Solution-side heat and mass transfer coefficient

The heat transfer coefficient h (W/m²K) at the solution side can be determined by the Nusselt number, which can be calculated by the following Gnielinski correlation [45, 46] with $\frac{RePrd_i}{L} < 100$:

$$Nu_{sol} = Nu_{lim} + \frac{0.085 \left[\frac{RePrd_i}{L} \right]}{1 + 0.047 \left[\frac{RePrd_i}{L} \right]^{0.67}} \left(\frac{v_b}{v_s} \right)^{0.14} \quad (1)$$

Where the subscripts 'b' and 's' refer to bulk and surface respectively. For the laminar flow inside the hollow fiber, the lower limit value of the Nusselt number (Nu_{lim}) is 3.658[45]. The relationship between Nusselt number and the heat transfer coefficient can be expressed as:

$$Nu_{sol} = \frac{hd_i}{\lambda} \quad (2)$$

Where d_i (m) is the fiber inside diameter, and λ (W/mK) is the thermal conductivity.

The mass transfer coefficient k (m/s) is related to the Sherwood number, which can be defined as:

$$Sh_{sol} = \frac{kd_i}{\psi_w} \quad (3)$$

The Sherwood number can be derived from the Leveque equation[47, 48] which is suitable for tube laminar flows ($Re < 2300$) with small fiber inside diameter ($d_i < 1.5mm$) and Graetz Number ($Gz = \frac{ud_i}{\psi_w L}$) over 25.

$$Sh_{sol} = 1.62 \left(\frac{d_i^2 u_{sol,i}^2}{L \psi_w} \right)^{\frac{1}{3}} \quad (4)$$

Where ψ_w (m²/s) represents water diffusivity in the solution inside the hollow fiber, d_i (m) is the fiber inside diameter, $u_{sol,i}$ (m/s) is the solution inlet velocity.

2.1.2 Air-side heat and mass transfer coefficient

According to [49], when air flow crosses a bundle of tubes with $Re_{D,max}$ in the range of 2000 to 40000 and Pr over than 0.7, the heat transfer coefficient at the air side is given by:

$$Nu_{air} = 1.13C_1 Re_{D,max}^m Pr^{\frac{1}{3}} \quad (5)$$

Where C_1 and m can be obtained from [49], and $Re_{D,max}$ can be calculated by:

$$Re_{D,max} = \frac{d_{h,air} u_{max}}{\nu} \quad (6)$$

Where u_{max} (m/s) is the maximum air velocity passing through the air channel, which can be calculated by:

$$u_{max} = \frac{u_{air,i} d_{h,air}}{d_{h,air} - d_o} \quad (7)$$

$d_{h,air}$ (m) is the equivalent hydraulic diameter of the air channel, which can be calculated as:

$$d_{h,air} = \frac{(1 - \varphi) d_c^2}{n_f d_o + d_c} \quad (8)$$

Where d_o (m) is the fiber outside diameter, d_c (m) is the module cross section diameter. n_f is the number of fibers included in the module, and φ is the packing fraction of the module, i.e. the ratio of the total fiber surface area to the PHFD module surface area,

$$\varphi = \frac{n_f \pi d_o^2}{\pi d_c^2} \quad (9)$$

As indicated by Zhang et al. [47], for the proposed PHFD configuration, at lower inlet air velocity, the air flow could be considered as laminar flow with the air side mass transfer correlation shown in the following equation:

$$Sh_{air} = (14.06\varphi^4 - 29.21\varphi^3 + 22.59\varphi^2 - 7.71\varphi + 1.03) Re^{0.33} Sc^{0.33} \tau_k \quad (10)$$

Where air side Schmidt number can be calculated as:

$$Sc_{air} = \frac{\mu_{air}}{\rho_{air} \psi_{air}} \quad (11)$$

Where μ_{air} (Pa • s) is the air dynamic viscosity, ρ_{air} (kg/m³) is the air density, and ψ_{air} (m²/s) is the moisture diffusivity in air and

$$\tau_k = 0.882\tau_f - 0.535 \quad (12)$$

where τ_f is the fractal dimension of the fiber packing. For the irregular and regular packing, the value of τ_f is 1 and 2, respectively, and the general value is 1.6 to 1.9[48].

2.1.3 Overall heat and mass transfer coefficients

The overall heat and mass transfer resistance should take into account the air-side resistance, solution-side resistance and hollow fiber resistance. The calculation equations were described in detail by Zhang et al.[48]. The overall heat transfer coefficient (h_{ov}) and the overall mass

transfer coefficient (k_{ov}) are estimated as the sums of the individual resistances, as shown in the following equations:

$$h_{ov} = \left(\frac{1}{h_i} \left(\frac{d_o}{d_i} \right) + \frac{\delta}{\lambda_m} \left(\frac{d_o}{\bar{d}} \right) + \frac{1}{h_o} \right)^{-1} \quad (13)$$

$$k_{ov} = \left(\frac{1}{k_i} \left(\frac{d_o}{d_i} \right) + \frac{\delta}{\psi_m} \left(\frac{d_o}{\bar{d}} \right) + \frac{1}{k_o} \right)^{-1} \quad (14)$$

where \bar{d} (m) is the average value of the fibers diameter, δ (m) is the thickness of the hollow fiber, d_o (m) and d_i (m) is the hollow fiber outside and inside diameter respectively. ψ_m (m²/s) is the effective mass diffusivity of the hollow fiber and λ_m (W/mK) is the effective thermal conductivity.

2.2 Heat and mass conservation equations

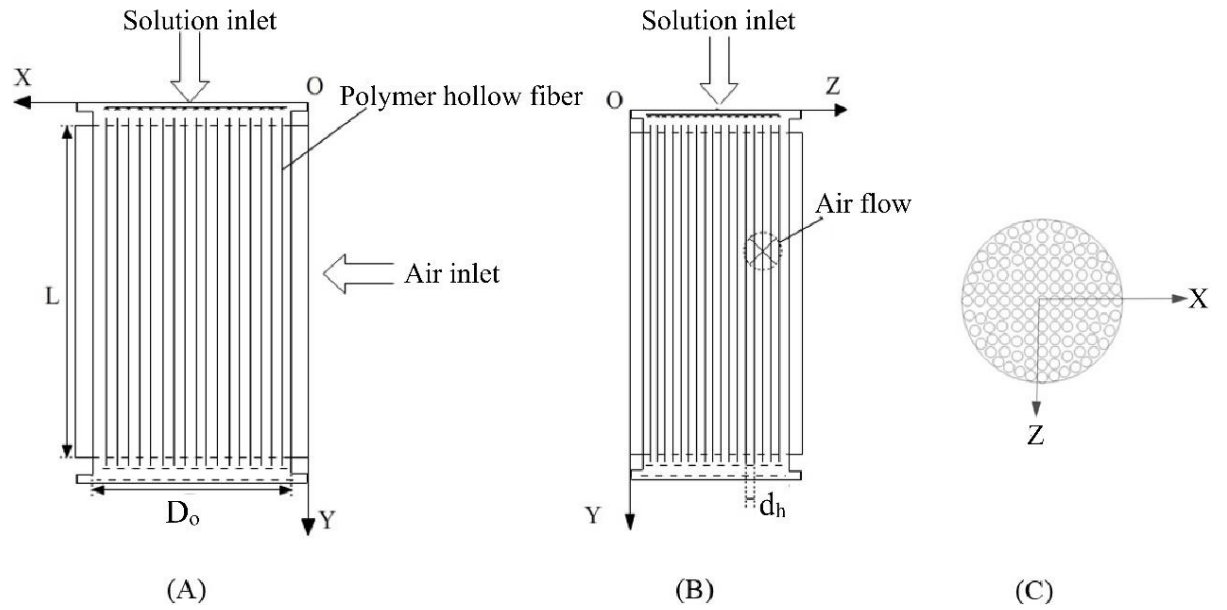


Fig. 2 The proposed polymer hollow fiber dehumidifier: (A) and (B) front view (C) section view

The proposed hollow fiber integrated crossflow desiccant dehumidifier is illustrated in Fig. 2. To simplify the numerical model, a series of basic assumptions were made:

- (1) According to the numerical simulation presented by Ge et al.[28], when the fibers are arranged in staggered pattern with solution side Re number less than 2000, the solution side flow can be consider as fully developed and laminar.
- (2) The physical properties of the air, solution, and the polymer hollow fiber, such as the specific heat, heat conductivity, etc. are constant.
- (3) The model is based on a two-dimensional cross-flow, with each fluid flowing in a single direction.
- (4) The axial water molecular diffusion, and the conduction of heat in the hollow fibers are

- ignored, since the Peclet number in both channels is larger than 20 [50, 51].
- (5) Moisture condensates only in the liquid side, and the latent heat arising from phase changes is also released only in the liquid side.
- (6) All the fibers inside the PHFD module are assumed to be uniformly distributed, therefore, the solution will be distributed uniformly through each single fibers.

2.2.1 Air-side and solution-side governing equations

The solution-side heat and mass conservation equations are given as

$$\left(\frac{\dot{m}_{sol}}{n_{eq} d_i} \cdot \frac{\partial T_{sol}}{\partial y} \cdot C_{p,sol} \right) = h_{ov}(T_{air} - T_{sol}) + h_{fg} \cdot k_{ov} \cdot \rho_a (\omega_{air} - \omega_{sol}) \quad (15)$$

$$\frac{\dot{m}_{sol}}{n_{eq} d_i} \cdot \frac{\partial X_{sol}}{\partial y} = k_{ov} \cdot \rho_a \cdot (\omega_{air} - \omega_{sol}) \quad (16)$$

where $\dot{m}_{sol}(kg/s)$ is the solution mass flow rate, $T_{sol}(^{\circ}C)$ and $T_{air}(^{\circ}C)$ are the solution temperature and air inlet temperature respectively, ω_{air} (kg moisture/ kg air) and ω_{sol} (kg KCOOH/kg solution) are the air humidity ratio and desiccant solution mass fraction, and n_{eq} is the equivalent number of fibers, which can be calculated as:

$$n_{eq} = \frac{A_{tot}}{d_c L} \quad (17)$$

Where $d_c(m)$ is the dehumidifier module cross section diameter, $L(m)$ is the height of the hollow fiber model, $A_{tot}(m^2)$ is the total heat exchange area, which can be calculated as :

$$A_{tot} = n \pi d_o L \quad (18)$$

The air-side governing equations are given as:

$$\frac{\dot{m}_{air}}{n_{eq} d_h} \cdot c_{p,air} \cdot \frac{\partial T_{air}}{\partial x} = h_{ov}(T_{sol} - T_{air}) \quad (19)$$

$$\frac{\dot{m}_{air}}{n_{eq} d_h} \cdot \frac{\partial \omega_{air}}{\partial x} + k_{ov}(\omega_{air} - \omega_{sol}) = 0 \quad (20)$$

where the $\dot{m}_{air}(kg/s)$ is the air flow rate, $c_{p,air}(J/kg K)$ is the air specific heat capacity.

2.2.2 Normalized equations

A range of dimensionless parameters can also be used:

The dimensionless temperature:

$$T^* = \frac{T - T_{air,i}}{T_{sol,i} - T_{air,i}} \quad (21)$$

The dimensionless humidity ratio:

$$\omega^* = \frac{\omega - \omega_{air,i}}{\omega_{sol,i} - \omega_{air,i}} \quad (22)$$

The dimensionless coordinates:

$$x^* = \frac{x}{d_c} \quad (23)$$

$$y^* = \frac{y}{L} \quad (24)$$

The dimensionless heat capacity ratios including sensible heat capacity ratio m_{sen} and latent heat capacity ratio m_{lat} are defined below:

$$m_{sen} = \frac{\dot{m}_{air} C_{p,air}}{\dot{m}_{sol} C_{p,sol}} \quad (25)$$

$$m_{lat} = \frac{\dot{m}_{air} h_{fg} (\omega_{sol,i} - \omega_{air,i})}{\dot{m}_{sol} C_{p,sol} (T_{sol,i} - T_{air,i})} \quad (26)$$

The number of transfer unit is defined by:

$$NTU = \frac{h_{ov} A_{tot}}{(\dot{m} c_p)_{air}} \quad (27)$$

And the number of mass transfer unit is defined by:

$$NTU_m = \frac{\rho_{air} k_{ov} A_{tot}}{\dot{m}_{air}} \quad (28)$$

The normalized formulae for the heat and mass conservation on the air side are:

$$\frac{\partial T_{air}^*}{\partial x^*} = NTU (T_{sol}^* - T_{air}^*) \quad (29)$$

$$\frac{\partial \omega_{air}^*}{\partial x^*} = NTU_m (\omega_{sol}^* - \omega_{air}^*) \quad (30)$$

Similarly, the normalized formulae for the heat and mass conservation on the solution side are:

$$\frac{\partial T_{sol}^*}{\partial y^*} = m_{sen} NTU (T_{air}^* - T_{sol}^*) + m_{lat} NTU_m (\omega_{air}^* - \omega_{sol}^*) \quad (31)$$

$$\frac{\partial \omega_{sol}^*}{\partial y^*} = M \frac{\partial T_{sol}^*}{\partial y^*} \quad (32)$$

where M is related to the dimensionless solution humidity ratio and the dimensionless solution temperature:

$$M = E_T \frac{T_{sol,i} - T_{air,i}}{\omega_{sol,i} - \omega_{air,i}} \quad (33)$$

where E_T is related to the solution humidity ratio and the solution temperature, which is defined as:

$$E_T = \left. \frac{\partial \omega_{sol}}{\partial T_{sol}} \right|_{\bar{x}_{sol}} \quad (34)$$

with

$$\omega_{sol} = 0.622 \frac{P_{sol}(X_{sol}, T_{sol})}{P_{atm} - P_{sol}(X_{sol}, T_{sol})} \quad (35)$$

where $P_{atm}(Pa)$ is the atmospheric pressure; $P_{sol}(Pa)$ is the solution's vapor pressure at a particular concentration and temperature, which can be obtained by;

$$P_{sol} = X_{sol} \cdot \exp^{\gamma} \cdot \exp^{P_{H_2O}} \quad (36)$$

where the parameters X_{sol} , γ , P_{H_2O} , are parameters related to desiccant solution and can be found in[52]. The concentration of the desiccant solution can be calculated via the correlation developed by Melinder [53], which relies on the temperature and density of the solution, as shown below:

$$X_{sol} = -253.148 + 0.04438563996 T_{sol} + 0.000162666247 T_{sol}^2 + 0.331709855 T_{sol} - 0.000079370267 \rho_{sol} \quad (37)$$

2.2.3 Boundary conditions

The solution side boundary conditions are:

$$T_{sol}^* = 1, \text{ at } y^*=0$$

$$\omega_{sol}^* = 1, \text{ at } y^*=0$$

The air side boundary conditions are:

$$T_{air}^* = 0, \text{ at } x^*=0$$

$$\omega_{air}^* = 0, \text{ at } x^*=0$$

2.4 Performance indices

Effectiveness is a key performance indicator of the dehumidifier. The sensible effectiveness ε_{sen} , latent effectiveness ε_{lat} , and total effectiveness ε_{tot} were used to evaluate the proposed model. The sensible effectiveness ε_{sen} is determined as the ratio of the air-temperature difference between the area-averaged outlet and the inlet, to the difference between the inlet solution temperature and the inlet air temperature (Eq. 38). The latent effectiveness ε_{lat} is the ratio of the area-averaged inlet and outlet air humidity difference to the humidity difference between the solution and the air at the inlet (Eq. 39);

$$\varepsilon_{sen} = \frac{T_{air,o} - T_{air,i}}{T_{sol,i} - T_{air,i}} \quad (38)$$

$$\varepsilon_{lat} = \frac{\omega_{air,o} - \omega_{air,i}}{\omega_{sol,i} - \omega_{air,i}} \quad (39)$$

The total effectiveness ε_{tot} is the ratio between the maximum and the actual energy transfer rates, which could be expressed as in (Eq. 40);

$$\varepsilon_{tot} = \frac{\varepsilon_{sen} + h_{fg} \frac{(\omega_{air,i} - \omega_{sol,i})}{(T_{air,i} - T_{sol,i})} \varepsilon_{lat}}{1 + h_{fg} \frac{(\omega_{air,i} - \omega_{sol,i})}{(T_{air,i} - T_{sol,i})}} \quad (40)$$

The moisture removal rate M (kg/s) is also a very important performance indicator of the liquid desiccant PHFD, and can be determined as:

$$M = \dot{m}_a (\omega_{air,i} - \omega_{air,o}) \quad (41)$$

2.5 Simulations

Eqs. (28) to (31) are the governing partial difference equations for the heat and mass transfer in the proposed model. They are two-dimensional and two-variable partial differential equations. A series of finite-differences iterations are performed in Matlab until the results converged. A grid independence test was performed in order to optimize the grids. It was found that grids of 60×60 were sufficient for this study, as the difference of the results is less than 1% compared to 60×120 grids. The process followed in this study is shown in the flowchart of Fig.3.

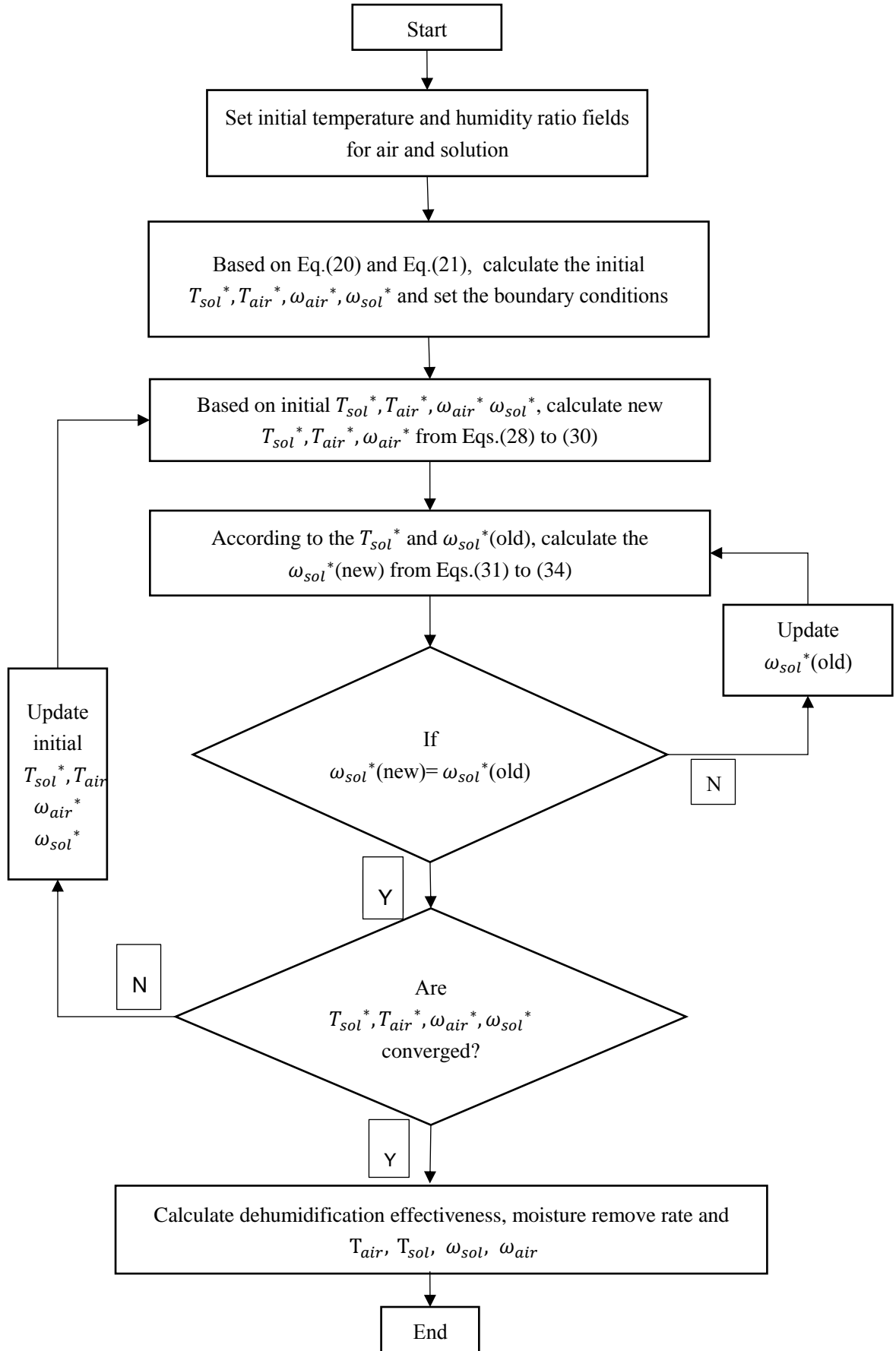
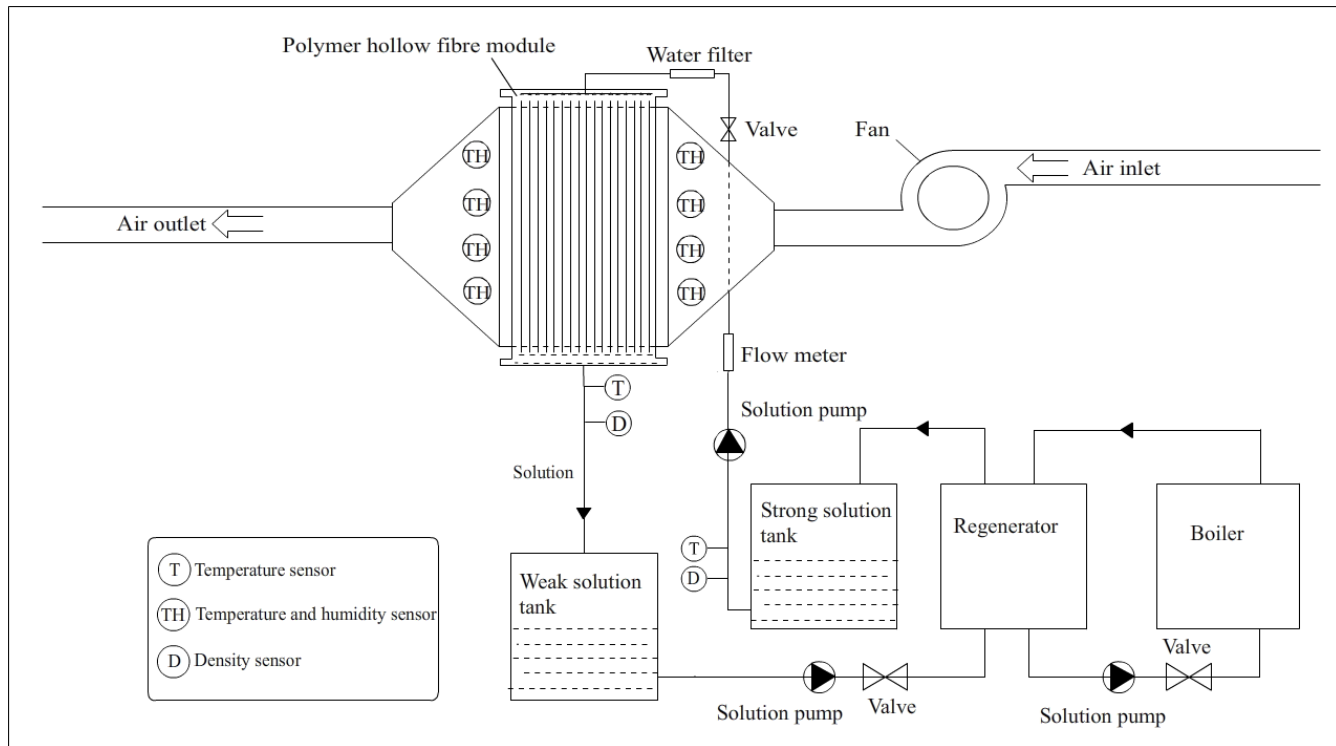


Fig.3. Flow chart for the simulation procedure

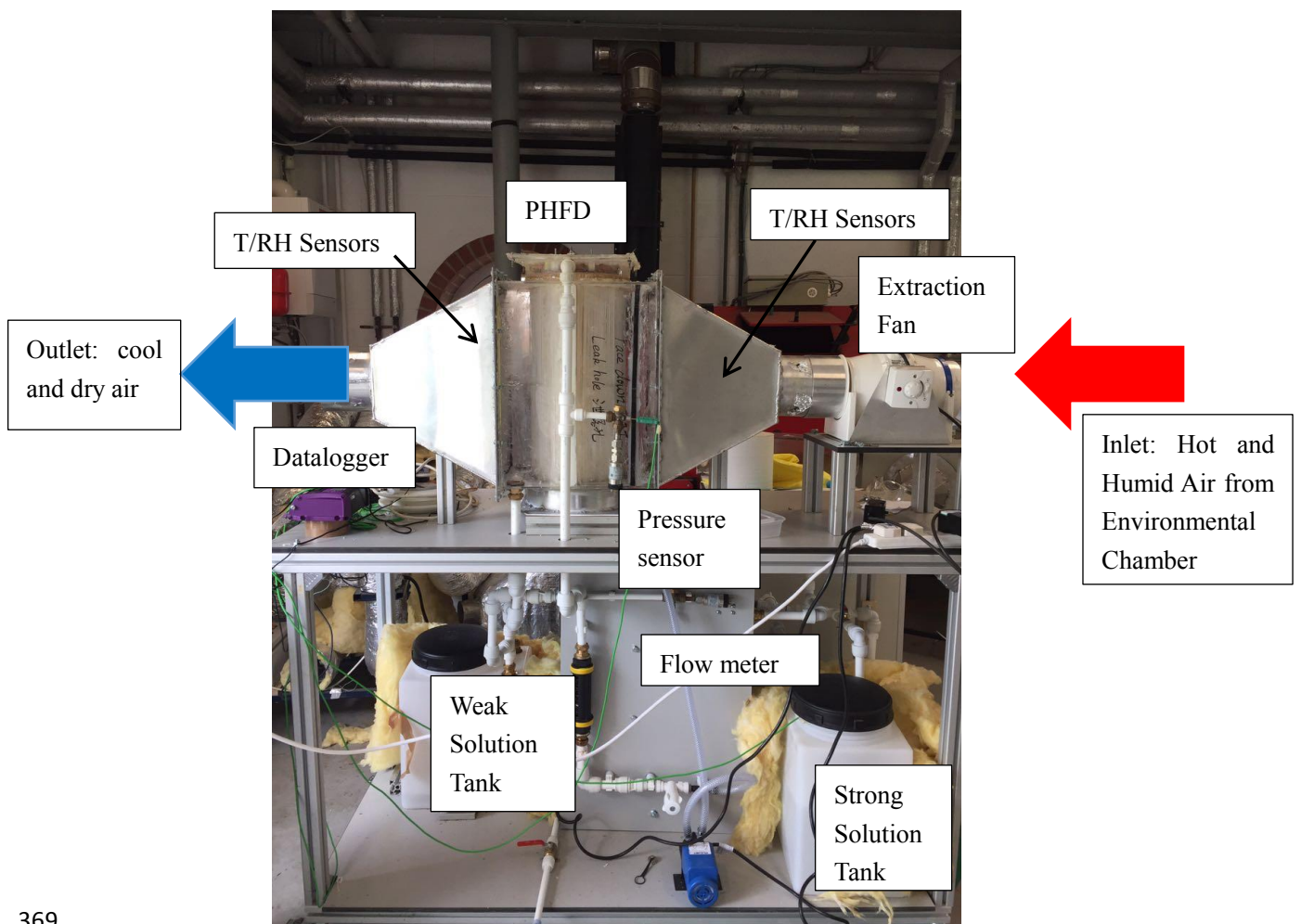
3. Experimental work

The experimental dehumidifier was assembled in the Marmot laboratory, University of Nottingham, UK. The schematic diagram and the experimental set up can be found in Fig.4 (A) and (B), respectively. The system includes the following major components: the polymer hollow-fiber dehumidifier, the air channel, a fan, two circulation pumps, two solution tanks and a water filter. The major component is the dehumidifier module with module cross section diameter of 0.2m and length of 0.6m. 5500 porous hollow fibers were combined as a bundle and attached on either end to a plastic disc by means of adhesive sealant. The polymer hollow-fiber dehumidifier was further integrated in a transparent plastic box to allow interactions with the incoming air. The aluminum air channel was attached to a centrifugal air fan with variable frequency, connected in turn to the environmental chamber with supply of humid and hot air of temperatures between 25°C and 40°C, and relative humidity of 0-75%. Two plastic tanks of an eight-liter capacity carried the strong and weak solutions of the liquid potassium. Located at the entrance of the PHFD, the water filter would help to eliminate any small particles entering into the liquid desiccant solution. A ball valve and a flow-meter were fixed at the entrance to the polymer hollow fiber module to control the solution flow rate inside the fibers. The physical and geometrical properties of the PHFD are listed in Table 2.

The experiments were conducted as follows. The intake air from the environmental chamber was directed inside the dehumidifier, once the environmental chamber had reached the required temperature and relative humidity. The strong KCOOH solution was pumped from the strong solution tank by a centrifugal pump (25W), to the desiccant solution inlet of the hollow fiber module, where it was sprayed from the top of the PHFD and was left to trickle down into the module. After being exposed to the inlet air, the dilute solution was collected into the relevant weak solution tank. It was then pumped into the regenerator, constructed as an aluminum-plate heat exchanger. Hot water (~80°C) was fed to the regenerator by a 3kW electrical boiler for the purpose of desiccant regeneration. Once the solution concentration achieved its desired ratio, it was returned to the strong-solution reservoir by a 25W single-phase centrifugal pump.



(A)



(B)

Fig. 4 Schematic diagram (A) and experimental set up (B) of the hollow fiber integrated liquid desiccant dehumidifier

Air temperature and humidity were measured by four dedicated monitoring devices (EK-H4, Sensirion, UK), which were placed by the inlet and the outlet of the air channel. The solution temperature was measured using K-type thermocouples. The air velocities in the air channel of the hollow fibre module were measured by a Testo anemometer. Its probe was distributed over several points around the outlet and inlet of the air tunnel. The dynamic pressure of the desiccant solution was measured by the Pressure transducers (Ge UNIK 5000). Finally, a DT500 data logger collected all the data from the above sensors. Detailed information about the measure sensors, for example, the measurement accuracy and measurement range are shown in Table 3. Uncertainty analysis of the experimental results was conducted following Moffat's method[54], and is shown in Fig. 5-12.

Table 2. Physical and transport properties of the polymer hollow-fiber dehumidifier

Property	Parameter	Values	Unit
Dehumidifier cross section diameter	d_c	0.20	m
Dehumidifier height	L	0.6	m
Number of fibers inserted	n_f	5500	
Fiber outside diameter	d_o	1.6	mm
Fiber inside diameter	d_i	1.4	mm
Pore size (nominal)		0.2	μm
Fibre porosity		0.6	
Packing density		832	m^2/m^3
Packing fraction	ϕ	0.32	
Fibre thermal conductivity	λ	0.17	W/mK
Solution concentration	X	57-67	%
Inlet air velocity	u_{air}	0.65-4.5	m/s
Solution mass flow rate	\dot{m}_{sol}	0.028-0.125	kg/s
Inlet air temperature	T_{air}	35-40	$^{\circ}\text{C}$
Inlet air relative humidity	ω_{air}	55-80	%
Specific heat of solution	C_{sol}	3.1	kJ/kg K
Dynamic viscosity of solution	μ_{sol}	5.1×10^{-3}	$\text{Pa} \cdot \text{s}$
Heat of evaporation	h_{fg}	2501	kJ/kg
Moisture diffusivity in air	ψ_{air}	2.82×10^{-5}	m^2/s
Effective mass diffusivity of the hollow fiber	ψ_m	1.2×10^{-5}	m^2/s
Water diffusivity in solution	ψ_w	0.3×10^{-2}	m^2/s
Number of heat transfer unit	NTU	0.46-4.4	
Number of mass transfer unit	NTU_m	0.28-2.8	

Table 3 Measurement devices and their accuracy

Instrumentation	Measured parameter	Measurement range	accuracy
Humidity and temperature sensors	Air (relative) humidity	0-90% RH	±2%
Humidity and temperature sensors	Air temperature	-40-125 °C	±0.3%
Testo thermo-anemometer	Air velocity	0–10 m/s	±5%
K-type thermocouple	Desiccant solution temperature	0-1100 °C	±0.75%
Datalogger DT500	Data Acquisition		±0.15%
Branna hydrometer 200 series	Solution density	1.0-1.6 g/m ³	±2%
Parker liquid flow indicator	Desiccant solution flow rate	0-5 litre/min	±5%

4. Results and discussion

4.1 Model validation

4.4.1 Experimental validation

The simulation results were validated against experimental results using 5 groups of experimentally obtained data. According to [49], since the ratio of hydraulic diameter of the air channel to the fiber outside diameter is equal to 2, the two parameters C_1 and m in Eq. (5) is chosen as 0.229 and 0.632, respectively. Under the various operating NTU and Cr^* conditions, the calculated and experimentally obtained outlet air temperature, specific humidity, outlet solution temperature, sensible effectiveness and latent effectiveness have been listed in Table 4 and Table 6. It is obvious that the proposed model matches well with the experimental results for both sensible effectiveness and latent effectiveness, with discrepancy in the range of 3.1-9.3% for sensible effectiveness and 2.5-8.9% for latent effectiveness. Therefore, this model in general can successfully predict the heat and mass transfer process in the PHFD.

406 Table 4 Comparisons between numerically obtained and experimentally obtained sensible
 407 effectiveness under various NTU ($Cr^*=0.13$)

Operating conditions		Parameters							
NTU	$T_{air,o}(exp)$	$T_{air,o}(num)$	Error(%)	$T_{sol,o}(exp)$	$T_{sol,o}(num)$	Error(%)	$\varepsilon_{sen}(exp)$	$\varepsilon_{sen}(num)$	Error(%)
0.4684	33.07	33.00	0.2	29.75	29.85	0.3	0.351	0.363	3.3
0.6012	32.74	32.59	0.5	29.86	29.93	0.2	0.4113	0.437	4.6
1.2764	31.19	31.32	0.4	30.27	30.21	0.2	0.693	0.668	3.1
3.045	30.29	30.21	0.3	30.59	30.67	0.3	0.856	0.927	7.6
4.4126	30.15	30.07	0.3	30.89	30.97	0.2	0.882	0.973	9.3

408 Table 5 Comparisons between numerically obtained and experimentally obtained latent
 409 effectiveness under various NTU_m ($m^*=0.75$)

Operating conditions		Parameters							
NTU_m	$\omega_{sol,o}(exp)$	$\omega_{sol,o}(num)$	Error(%)	$\omega_{air,o}(exp)$	$\omega_{air,o}(num)$	Error(%)	$\varepsilon_{lat}(exp)$	$\varepsilon_{lat}(num)$	Error(%)
0.2803	0.0117	0.0118	0.3	0.0192	0.0190	1.0	0.191	0.196	2.5
0.8318	0.0122	0.0125	2.4	0.0164	0.0160	2.4	0.478	0.514	7.0
1.3232	0.0124	0.0129	4.0	0.0149	0.0144	4.0	0.613	0.664	7.6
1.8631	0.0126	0.0132	4.8	0.0140	0.0135	3.5	0.702	0.748	6.5
2.8631	0.0127	0.0134	5.5	0.0135	0.0127	5.9	0.749	0.822	8.9

410

411 4.1.2 Analytical Validation

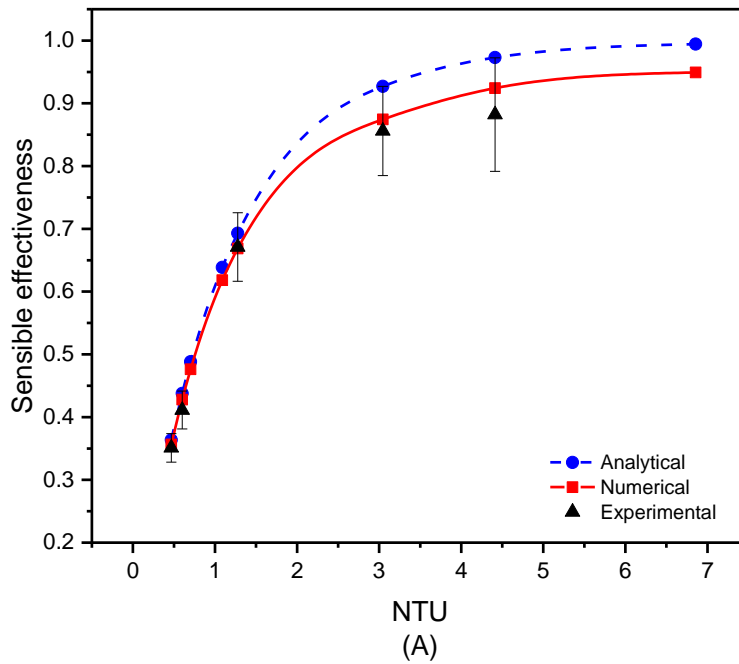
412 Analytical solutions for an enthalpy exchanger considering a membrane core have been
 413 reported in various works [55, 56]. According to these, the sensible effectiveness and latent

effectiveness of cross flow is given by the NTU- ϵ method. Those parameters are functions of four dimensionless parameters; the former are NTU and Cr^* and the latter are NTU_m and m^* [36]:

$$\epsilon_{sen} = 1 - \exp \left[\frac{\exp(-NTU^{0.78} Cr^*) - 1}{NTU^{-0.22} Cr^{*-1}} \right] \quad (42)$$

$$\epsilon_{lat} = 1 - \exp \left\{ \frac{NTU_m^{0.22}}{m^{*-1}} \left[\exp(-m^* NTU_m^{0.78}) - 1 \right] \right\} \quad (43)$$

The results of the analytical solutions in Fig. 5 show a trend consistent with the numerical modelling results. As it can be seen in Fig. 5, a good agreement between numerical and experimental results occurs when the inlet air flow rate is less than 0.02kg/s. As the value of NTU and NTU_m increases, the two curves start to deviate. This is because the higher the NTU and NTU_m , the lower the air velocity and solution mass flow rate. With the 5500 hollow fibers imbedded in one module, the inner parts of the hollow fibers will have less opportunity to be exposed to the incoming air, leading to a decrease in heat transfer performance.



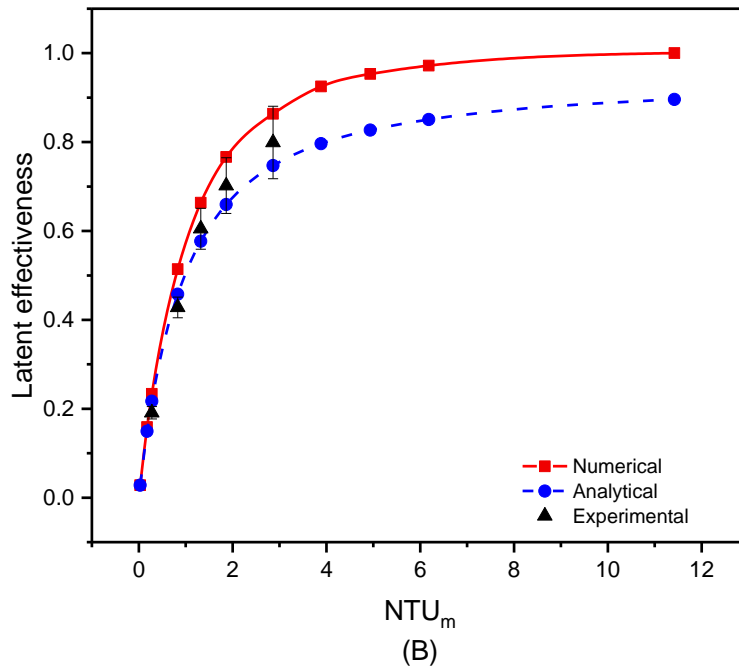


Fig. 5 Variations of sensible effectiveness (A) and latent effectiveness (B) under various NTU_m based on experimental data, numerical results and analytical solutions.

4.1.3 Comparison with previous studies

This model is further compared with numerical results reported in the literature[57]. The validation considers a crossflow membrane dehumidifier operating under the inlet air temperature from 25.7 °C to 35.2 °C, specific humidity of 0.015kg/kg to 0.022kg/kg and inlet air mass flow rate of 7.55 to 15.65kg/h using LiCl as the desiccant solution. Table 6 shows the comparisons between Zhang's model[57] and the model proposed in this paper under the above conditions. It can be found that the results of the outlet air temperature and the outlet solution temperature obtained from the model presented in this paper, are highly consistent with the results of Zhang's model[57], with maximum discrepancy of 2.9% for the outlet solution temperature, and 1.6% for the outlet air temperature.

To summarize, the proposed numerical model was shown to be consistent with experimental results, the analytical solution, and results from the literature. Hence, this model could be adopted to analyze the working performance of the PHFD studied in this research.

Table 6 Comparisons between Zhang's model [57] and the model proposed in this paper under the same conditions

Operating conditions					Parameters				
\dot{m}_{sol}	\dot{m}_{air}	$T_{air,i}$	$T_{sol,i}$	$T_{air,o}$	Error(%)	$T_{sol,o}$	Error(%)		
				Zhang's model	This model		Zhang's model	This model	
9.69	6.36	33.9	24.9	25.99	25.65	1.3	32.44	32.90	1.4
9.75	8.67	35.2	25.3	28.04	27.72	1.1	36.89	37.51	1.8
9.66	12.22	34.9	25.2	29.58	29.54	0.1	37.78	38.52	1.9

8.79	15.65	33.7	25.2	30.37	30.83	1.6	36.72	37.86	2.9
5.29	12.45	33.8	25.5	33.3	33.79	1.2	40.42	40.23	0.5
10.19	7.55	35.3	24.5	26.5	26.09	1.5	35.27	35.94	1.9
9.53	7.45	32.8	24.6	26.37	25.95	1.2	33.68	34.08	1.0
9.67	7.43	29.8	24.6	26.39	25.73	2.2	32.39	32.59	0.6
9.67	7.45	27.2	25.6	26.51	26.44	0.3	30	31.17	3.6
9.45	7.66	25.7	25.4	26.31	26.22	0.3	29.46	30.26	2.7

4.2 Effect of the inlet air conditions

According to the numerical analysis results, the inlet air conditions (i.e. inlet air velocity $V_{air,i}$, and temperature $T_{air,i}$) are crucial parameters of the proposed PHFD. Fig 6-8 show the variations of 4 parameters: sensible effectiveness, latent effectiveness, outlet air temperature and specific humidity difference under various air velocities. As shown in Fig. 6, with increasing air velocity, the latent heat capacity ratio (m_{lat}) and sensible heat capacity ratio (m_{sen}) will increase while the NTU_m and NTU will decrease. As demonstrated in Fig. 7, a higher inlet air velocity will cause a rise of the outlet air temperature and the specific humidity difference between the inlet and the outlet air. This results in the increase of the sensible and latent effectiveness, as shown in Fig.8. For example, at the inlet air relative humidity of 60% and dry bulb temperature of 35°C, when the inlet air velocity increases from 1.5m/s to 4.5m/s, the specific humidity difference between the inlet air and the outlet air are 0.0040kg/kg, 0.0030kg/kg, 0.0022kg/kg, 0.0018kg/kg respectively. The sensible and latent effectiveness decreases from 0.381 to 0.03 and 0.383 to 0.178, respectively. This is because the higher air velocity leads to the reduction of the contact duration between the incoming air and the desiccant solution inside the PHFD. This results in less effective heat and mass transfer, which is reflected in the reduced sensible and latent effectiveness, as shown in Fig.8.

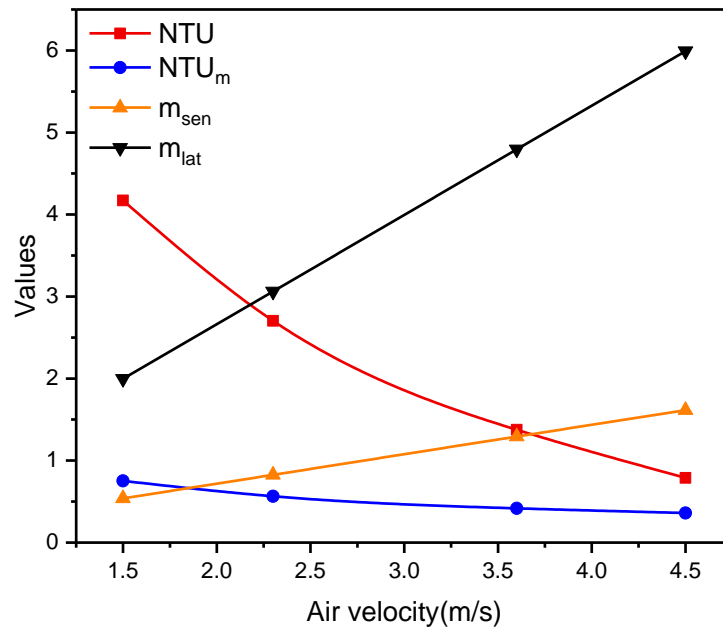
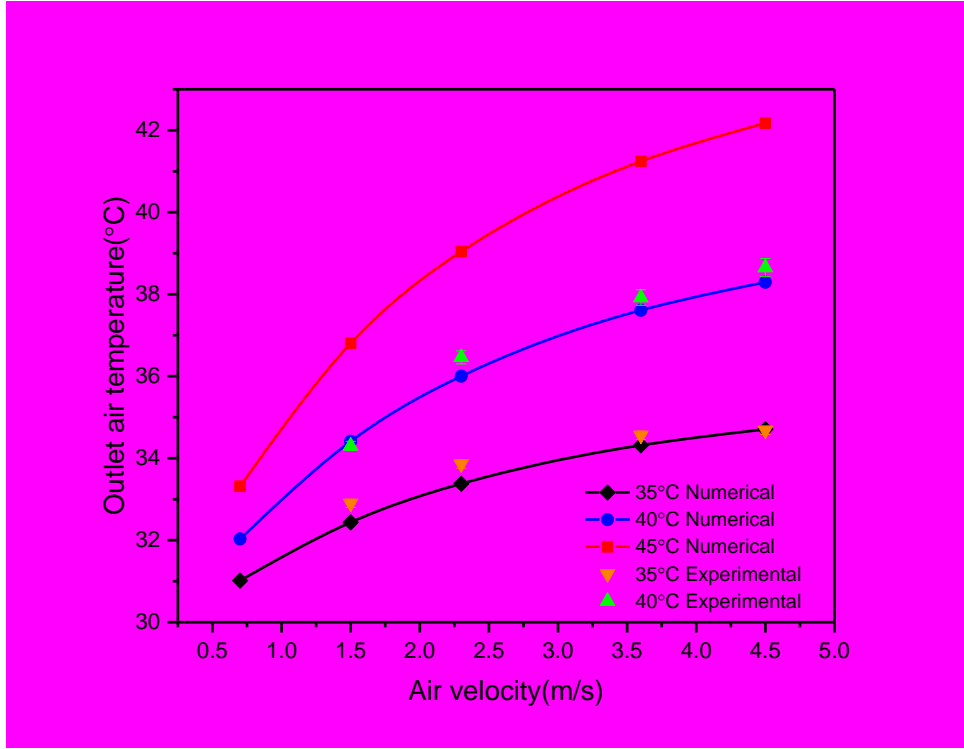
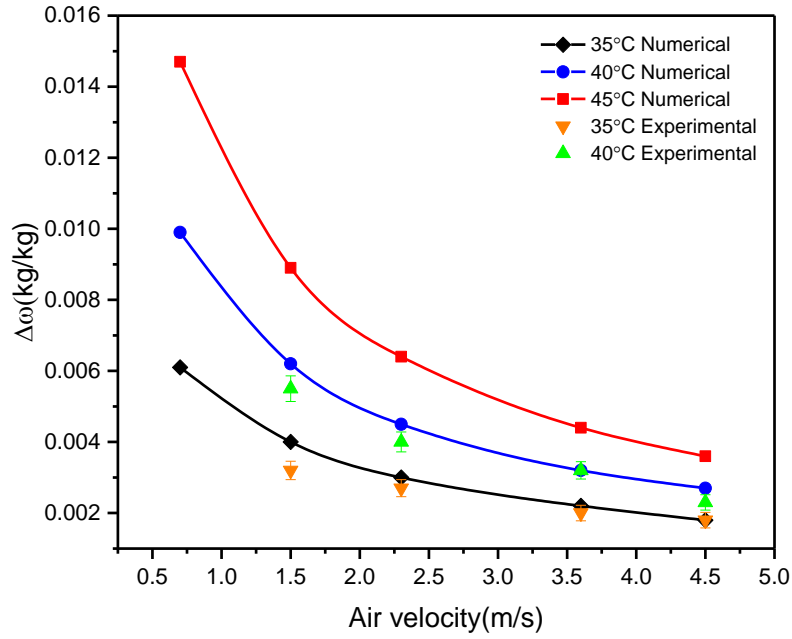


Fig. 6 The dimensionless parameters variations under different air velocities ($T_{air,i} = 35^\circ\text{C}$,

$$T_{sol,i}=29.5^{\circ}\text{C}, \quad \dot{m}_{sol,i}=0.028\text{kg/s}, \quad RH_{air,i}=60\%, \quad X_{sol}=62\%$$



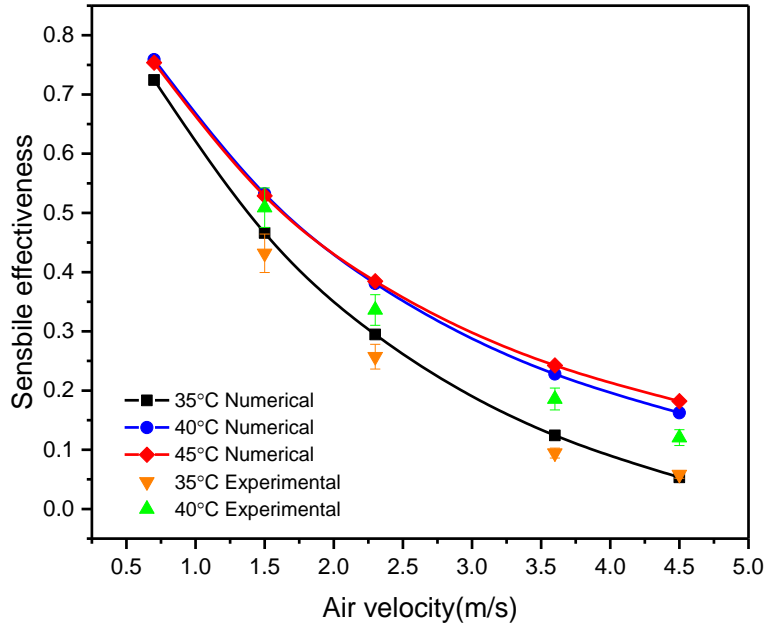
(A) (error bars in 35 degree C experimental results should be shown in this figure, the same as 40 degree C's error bar)



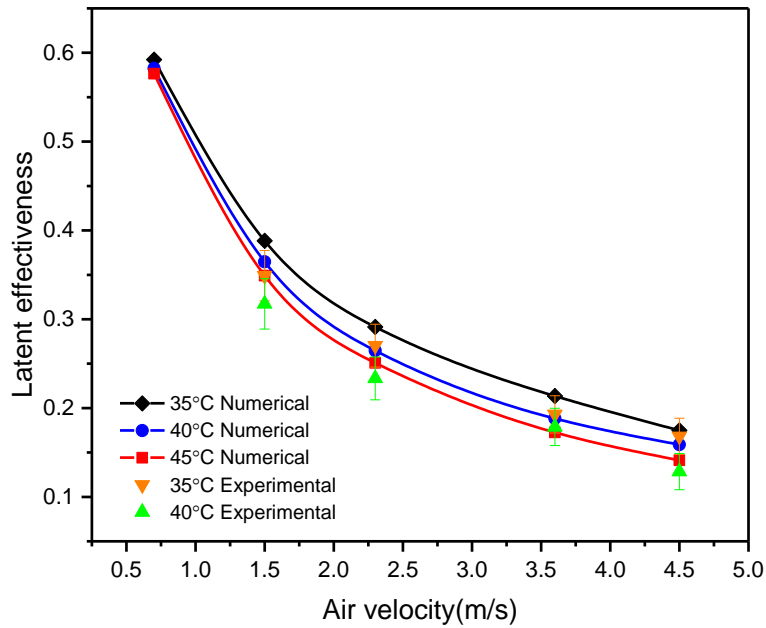
(B)

Fig. 7 The numerically obtained outlet air temperature (A), and specific humidity difference

479 (B), under various air velocities ($T_{sol,i}=29.5^{\circ}\text{C}$, $\dot{m}_{sol,i}=0.028\text{kg/s}$, $\text{RH}_{air,i}=60\%$, $X_{sol}=62\%$)



480 (A)



482 (B)

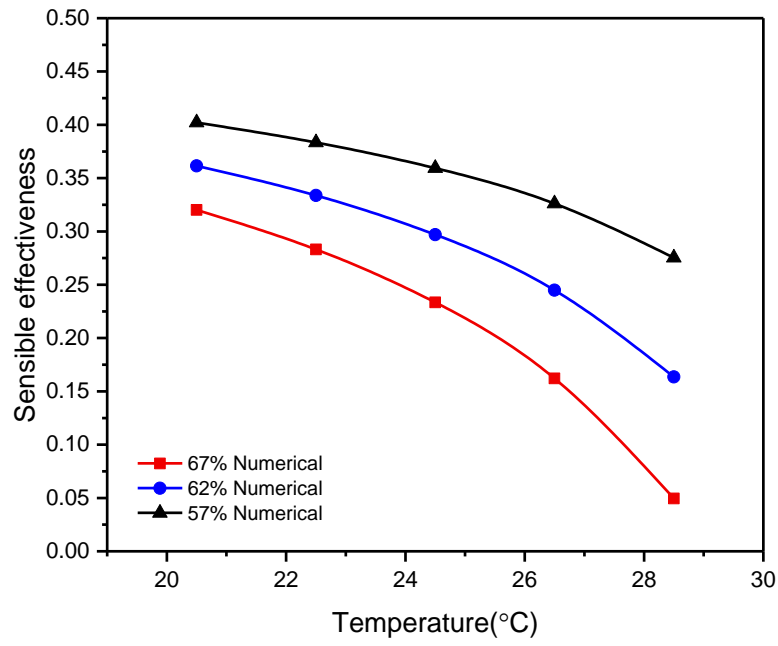
483 Fig. 8 The numerically obtained sensible effectiveness (A), and latent effectiveness (B), under
484 different inlet air velocities ($T_{sol,i}=29.5^{\circ}\text{C}$, $\dot{m}_{sol,i}=0.028\text{kg/s}$, $\text{RH}_{air,i}=60\%$, $X_{sol}=62\%$)

485
486
487 Further observation of the results shown in Fig. 8(A) reveals that at the fixed solution
488 concentration and inlet air velocity, the sensible effectiveness will increase at a higher air

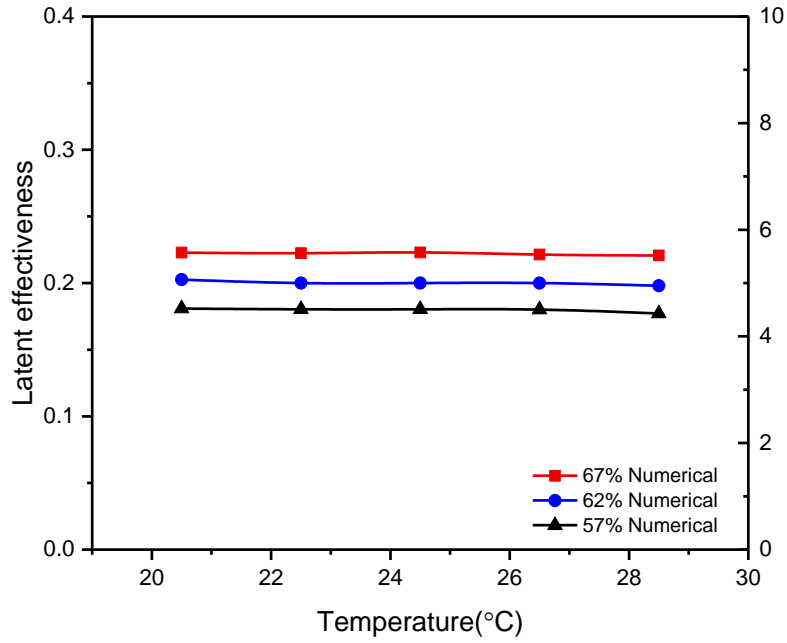
temperature. For instance, when the air velocity is fixed at 3.6m/s, for the inlet air temperature of 35°C, 40°C and 45°C, the sensible effectiveness is 0.12, 0.23 and 0.24, respectively. In contrast, as depicted in Fig. 8 (B), when the solution concentration and the inlet air velocity are fixed, a higher inlet air temperature results in lower latent effectiveness. For instance, the latent effectiveness only decreases by 1.6% and 1% respectively when the inlet air temperature increases from 35°C to 40°C and 40 to 45°C at 0.7m/s air velocity, which is negligible. On the contrary, $\Delta\omega$ increases with the improvement of inlet air temperature when the inlet air velocity is fixed at 0.7m/s. The reason is that the increase of the inlet air temperature will lead to higher specific humidity, while the inlet equilibrium humidity of the solution remains unchanged and increases the vapor pressure difference indirectly.

4.3 Effect of the liquid desiccant solution inlet conditions

The temperature of the solution and its concentration also play crucial roles in the dehumidification performance. Fig.9 shows the variations of the sensible and latent effectiveness under several inlet solution temperatures at various concentrations. As it can be found from Fig.9 (A), the sensible effectiveness drops with the increase of the solution temperature. For example, at a 57% concentration, the sensible effectiveness varies from 0.4 to 0.3 when the solution temperature changes from 20.5°C to 28.5°C. It should be noted that at higher solution temperatures, high concentration solutions are more sensitive to temperature changes. For instance, as the temperature of the solution rises from 26.5°C to 28.5 °C, the sensible effectiveness at a 57% concentration drops by 15%. In contrast, when the concentration is 62%, the corresponding decrease is 32%. In Fig.9(B), it can be seen that the latent effectiveness almost remains constant as the solution temperature rises. For instance, at a 62% concentration, the latent effectiveness is 0.203, 0.200, 0.200, 0.200, 0.198 at the solution temperature of 20.5°C, 22.5°C, 24.5°C, 26.5°C, 28.5°C, respectively. This is because, according to Eq. (35), the solution equilibrium humidity (K_{COOH}) is related to its temperature and concentration. Although the vapor pressure will naturally increase with the solution temperature, the solution equilibrium humidity will also increase, and will thus reduce both the nominator and denominator of Eq. (35). In addition, lower solution concentration leads to lower latent effectiveness, for example, at 26.5°C, the latent effectiveness is 0.22, 0.20, and 0.18 for the concentration ratios of 67%, 62%, 57%, respectively.



(A)



(B)

Fig. 9 Variations of sensible effectiveness (A), and latent effectiveness (B), for several inlet solution temperatures at various solution concentrations ($T_{air,i}=35^{\circ}\text{C}$, $\text{RH}_{air,i}=60\%$, $V_{air,i}=3.6\text{m/s}$, $\dot{m}_{sol,i}=0.028\text{kg/s}$)

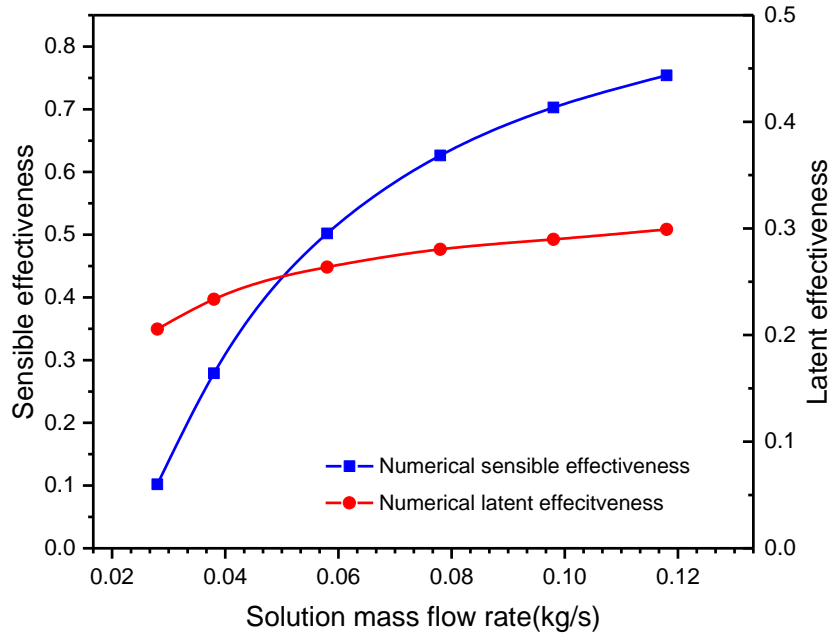


Fig 10 Variations of latent and sensible effectiveness with the solution mass flow rate ($T_{air,i}=35^{\circ}\text{C}$, $T_{sol,i}=29.5^{\circ}\text{C}$, $RH_{air,i}=60\%$, $X_{sol}=62\%$, $V_{air,i}=3.6\text{m/s}$)

Fig.10 shows the relationship between solution mass flow rate and effectiveness, including sensible effectiveness and latent effectiveness. With the increase of the solution mass flow rate, the sensible effectiveness will increase dramatically. For instance, when the air mass flow rate increases from 0.02kg/s to 0.012kg/s , the sensible effectiveness shows a 7.7 times increase. This is because a higher solution flow leads to a lower average solution temperature, and the outlet air temperature will decrease. As for the latent effectiveness, this will also increase with the solution mass flow rate. For example, the sensible effectiveness only increases by 46% when the solution flow rate rises from 0.02kg/s to 0.012kg/s . This is because the increase of the solution mass flow will result in the lower average equilibrium vapour pressure of the desiccant solution, and a higher mass transfer capacity will be obtained. It should be noted that when the solution mass flow rate is over 0.08kg/s , the growth rate of both the sensible and latent effectiveness will drop. As far as the sensible effectiveness is concerned, the reason for this is that the average solution temperature has a limit value, which is infinitely close to the initial solution temperature when the solution mass flow rate is much bigger than the air flow rate, hence the heat transfer driving force becomes weaker. For the latent effectiveness, the larger the solution mass flow rate, the more moisture will be absorbed by the desiccant, and the value of the air-specific humidity will be close to the equilibrium specific humidity of the desiccant solution, hence the ability of absorbing the moisture will become weaker.

4.4 Effects of the dimensionless parameters

The influences of the air to solution specific humidity ratio ω_r^* on the outlet air temperature, the sensible effectiveness, the specific humidity difference, the moisture removal rate, the latent effectiveness, and the total effectiveness are demonstrated in Figs. 11-13. The other initial air and solution conditions were invariable, the air velocity at the inlet was fixed at 0.7m/s , the

inlet air temperature was fixed at 35°C, and the inlet solution mass flow rate was 0.028 kg/s. As shown in Fig. 11, the air temperature at the outlet rises from 30.6°C to 31.8°C (an increase of 3.9%) and the sensible effectiveness drops from 0.79 to 0.57 (a fall of 22%) when the ω_r^* varies between 1.46 and 2.12. Inspection of Fig. 12 reveals that both the air specific humidity difference and the moisture removal rate both increase when the ω_r^* increases. For instance, the air specific humidity difference is 0.0053 kg/kg, 0.0065 kg/kg, 0.0079 kg/kg, 0.0089 kg/kg, 0.0098 kg/kg and 0.0106 kg/kg at ω_r^* of 1.46, 1.62, 1.78, 1.88, 1.99 and 2.12, respectively, and the rate of moisture removal rised by 104% (from 0.21kg/s to 0.43kg/s) at each ω_r^* . The reason is that a higher ω_r^* reflects a higher water vapor pressure. No matter whether the inlet air specific humidity increases or the inlet solution concentration decreases, a greater vapor pressure difference between incoming air and desiccant solution is built. This leads to the solution attracting more moisture from the inlet air, which increases the specific humidity difference between the inlet air and the outlet air. When the desiccant solution absorbs more vapor, a higher amount of latent heat will be released. This results in a smaller temperature difference between the incoming air and the desiccant solution, which makes the temperature drop gradually.

As shown in Fig. 13, the impact of the air to solution specific humidity ratio on the latent effectiveness is negligible. For example, the latent effectiveness remains around 0.61, when ω_r^* changes from 1.45 to 2.15. On the other hand, the total effectiveness decreases with the increase of ω_r^* . This is because although the air-specific humidity or solution equilibrium humidity increase dramatically with the rise of ω_r^* , the air specific humidity difference between the air and the solution at the inlet also grows. Thus, the latent and total effectiveness are not affected by ω_r^* .

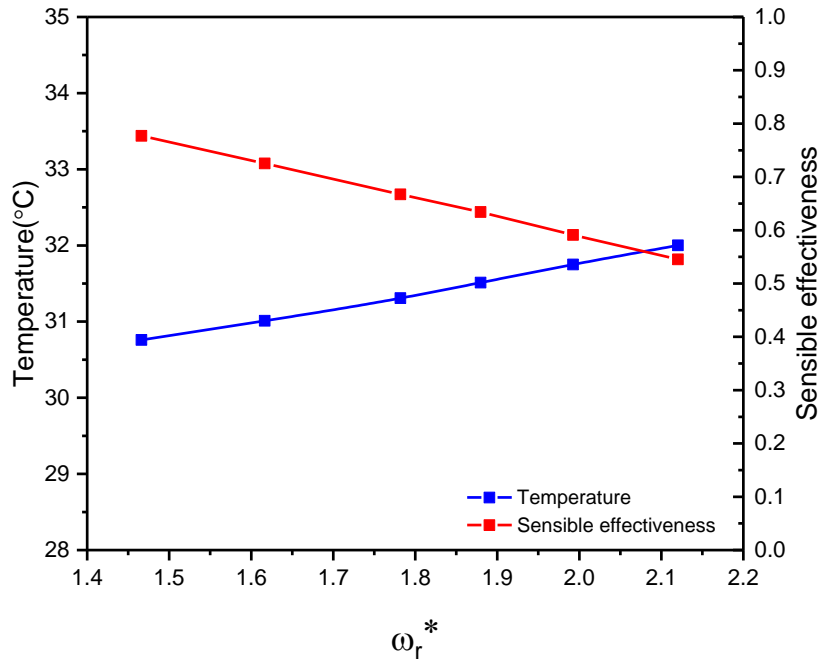


Fig 11 Variation of the outlet air temperature and sensible effectiveness with the air to solution specific humidity ratio ($T_{air,i} = 35^\circ\text{C}$, $T_{sol,i} = 29.5^\circ\text{C}$, $\dot{m}_{sol,i} = 0.028\text{kg/s}$, $V_{air,i} = 3.6\text{m/s}$)

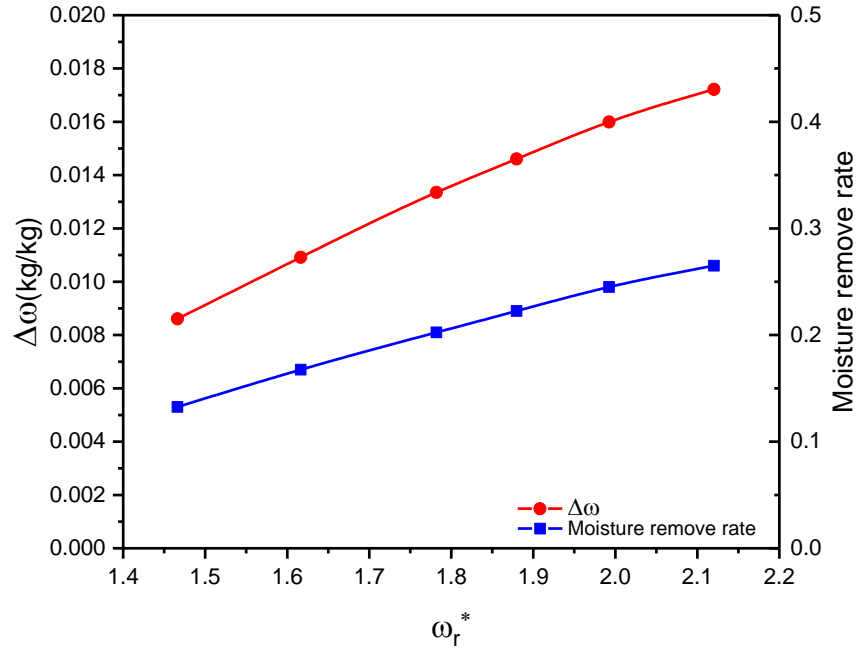


Fig 12 Variation of the specific humidity difference and moisture removal rate with the air to solution specific humidity ratio ($T_{air,i}=35^\circ\text{C}$, $T_{sol,i}=29.5^\circ\text{C}$, $\dot{m}_{sol,i}=0.028\text{kg/s}$, $V_{air,i}=3.6\text{m/s}$)

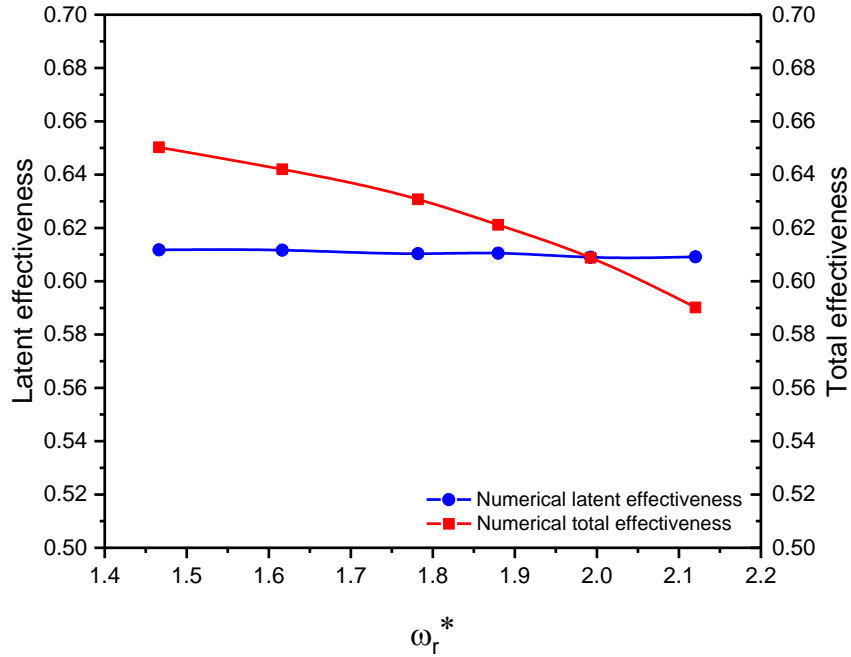


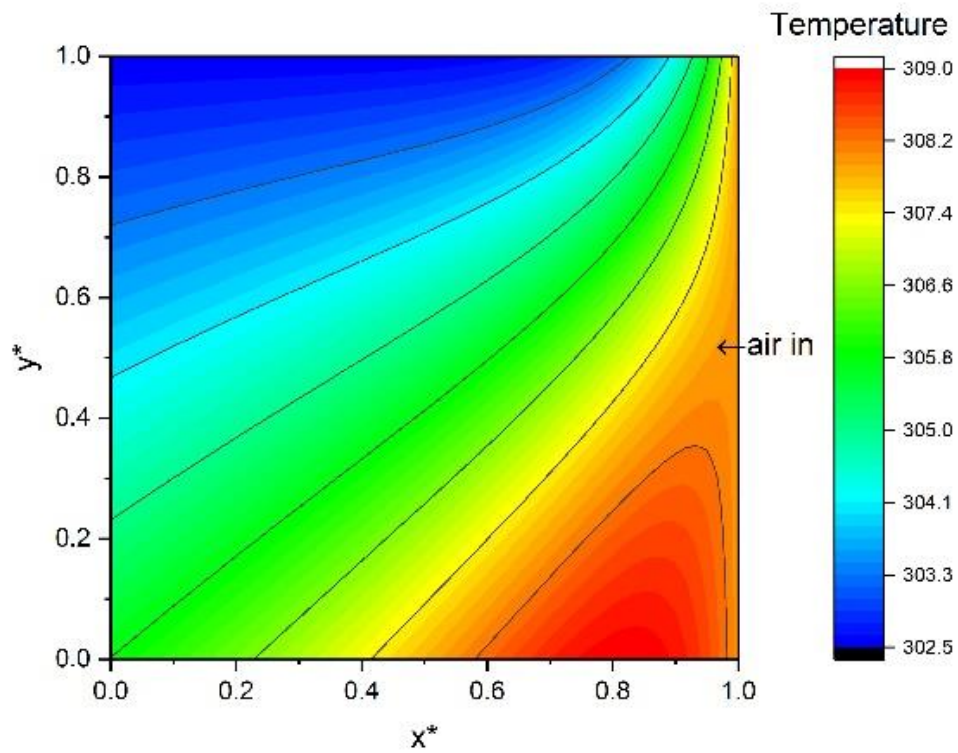
Fig 13 Variation of the latent effectiveness and total effectiveness with the air to solution specific humidity ratio ($T_{air,i}=35^\circ\text{C}$, $T_{sol,i}=29.5^\circ\text{C}$, $\dot{m}_{sol,i}=0.028\text{ kg/s}$, $V_{air,i}=3.6\text{ m/s}$)

To summarize, the variation of air velocity has a strong impact on T_{ao} , ω_{ao} , NTU, NTU_m, \dot{m}_{sen} , \dot{m}_{lat} , and has a significant effect on the latent effectiveness and the sensible effectiveness. The sensible effectiveness and total effectiveness are less related to ω_r^* . The moisture removal rate and the sensible effectiveness also change significantly with the variations of ω_r^* . In addition,

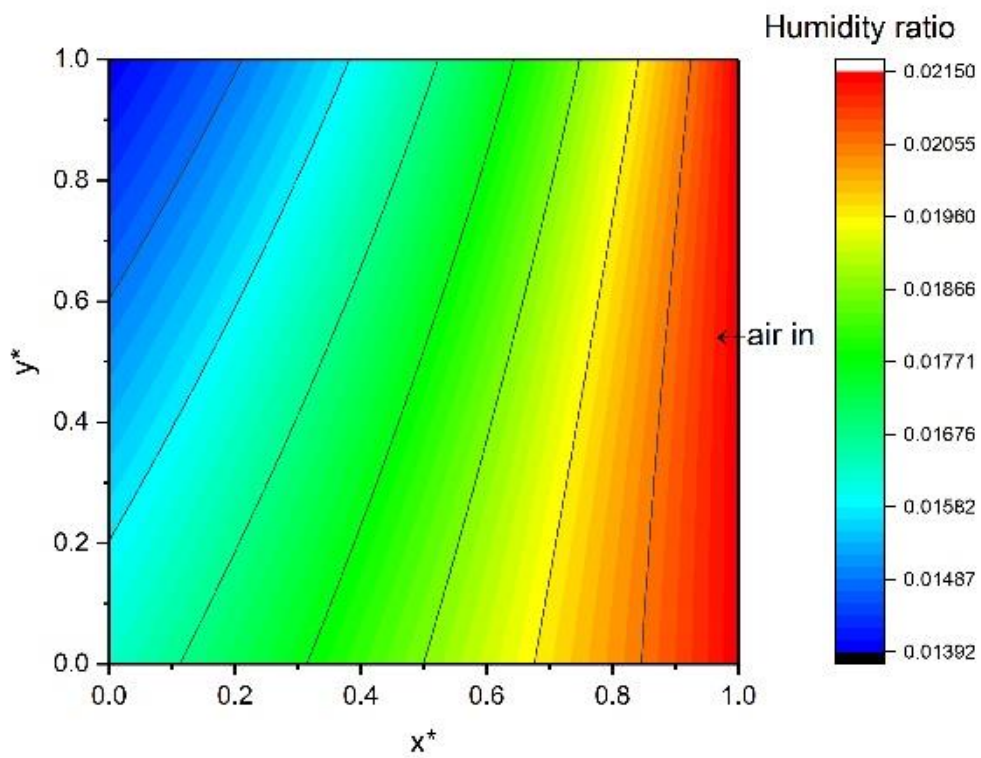
the change of air specific humidity difference and the inlet and outlet air temperature difference are closely related to ω_r^* . This implies that changes of the ω_r^* within a certain range (i.e. 1.45 to 2.15) is preferable for increasing the dehumidification performance without reducing the latent effectiveness.

4.5 Temperature and humidity contour

Temperature and humidity ratio contours of both the air and the solution are plotted in Figs.14-15, based on the modeling results. The inlet air temperature, specific humidity ratio and mass flow rate are 35°C, 0.0215kg/kg and 0.0407kg/s, respectively, and the inlet solution temperature is 29.5°C, while the inlet equilibrium humidity ratio of the solution is 0.01076kg/kg, and the solution mass flow rate is 0.028 kg/s. In Figs.14-15, the bottom boundary line indicates the solution inlet and the right boundary line indicates the air inlet. Fig. 14 indicates that the air specific humidity decreases from the inlet to the outlet. It is interesting to observe that the drop rate of the air specific humidity slows down from the solution inlet to the solution outlet. This is mainly because at the solution inlet, the solution has the lowest equilibrium humidity ratio, which means that the solution can maximally absorb moisture from the incoming air. In contrast, at the outlet, the desiccant solution has a much higher equilibrium humidity ratio. As for the air flow, the temperature decreases along the x axis, and reaches the lowest temperature (top right corner of the model) at nearly 29.5°C. It should also be noted that at the corner between solution outlet and air inlet, the air temperature is slightly higher than the inlet temperature. This is due to the accumulation of latent heat released by moisture, and sensible heat from the air, which leads to the rise of the solution temperature as indicated in Fig. 14. As seen, the solution temperature and equilibrium humidity ratio both increase from solution inlet to solution outlet and reach the highest value (36.3°C and 0.01606kg/kg, respectively) at the corner between solution outlet and air inlet of the model. The rate of change (from solution inlet to solution outlet) slows down from the air inlet to the air outlet.



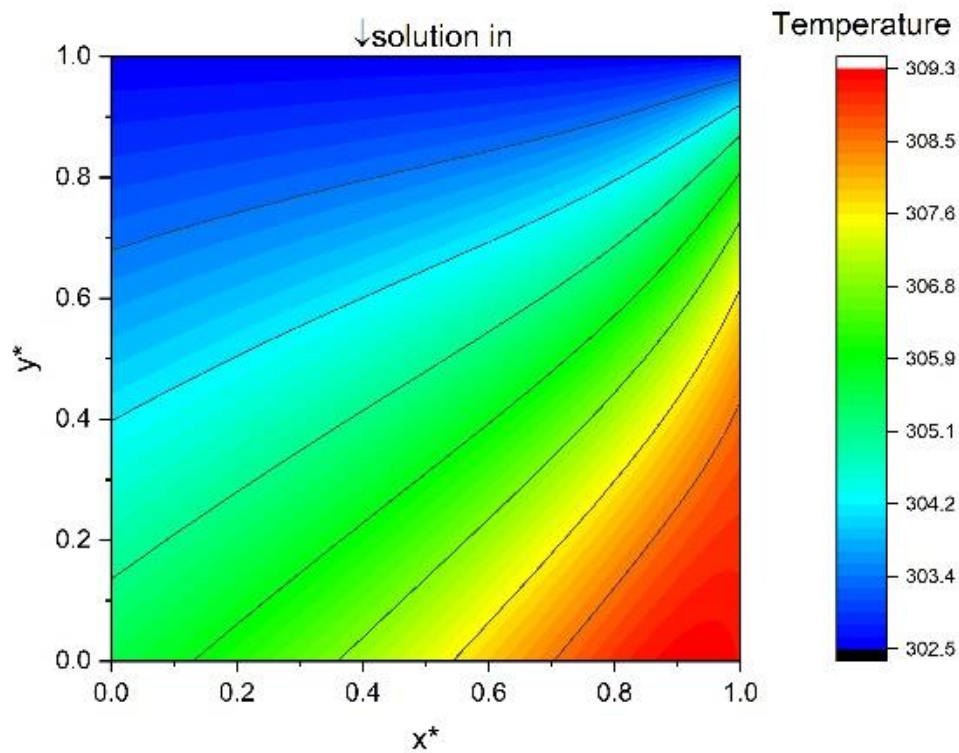
615



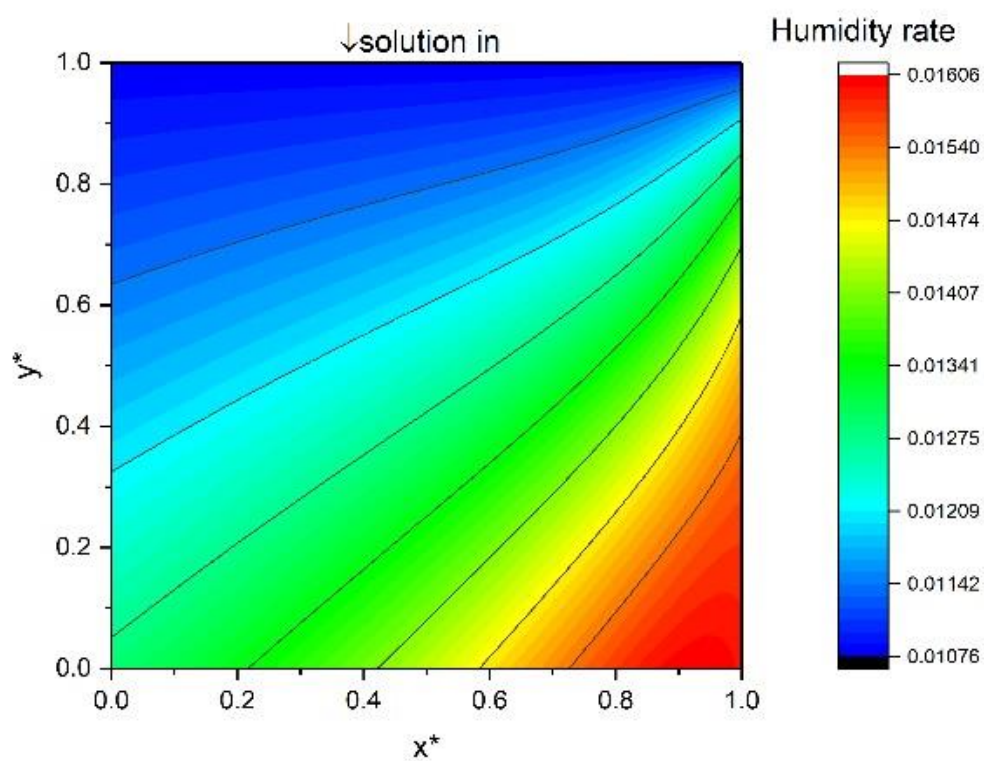
616

617

Fig. 14 Air temperature and humidity ratio contour



618



619

620

Fig. 15 Solution temperature and equilibrium humidity ratio contour

621

622 **5. Application**

Fig. 16 depicts the simulated outlet air temperature and specific humidity as a function of the number of fibers in the proposed liquid desiccant PHFD, with the inlet air RH=60% and inlet air temperature fixed at 30°C, 35°C and 40°C, respectively. Calculations have been performed based on the square cross section of the dehumidifier with fiber numbers increasing from 400 to 8100. Fig. 16 shows two different solutions to air mass flow ratios which represent the two lowest air velocities ($\dot{m}_{sol}/\dot{m}_{air}=10$ and $\dot{m}_{sol}/\dot{m}_{air}=5$) applied in this research. Table 7 summarizes the outlet air conditions together with the sensible and latent effectiveness at the inlet air temperature of 35°C, specific humidity of 0.0215kg/kg and solution inlet temperature of 25°C. It can be seen that as the fiber number goes beyond 3000, the outlet air temperature, as well as the sensible and latent effectiveness maintain roughly the same value. This indicates that the optimum fiber number could be identified at around 3000 for lower air mass flow rate, which is associated with more effective heat and mass transfer. As the inlet air mass flow rate increases, the incoming air will have less time to be exposed to the desiccant solution, therefore more fibers with larger surface areas are required to obtain higher sensible and latent effectiveness.

Fig. 16 and Table 7 can be useful in the practical design stage of polymer hollow fiber integrated liquid desiccant dehumidification systems. It can help designers to obtain the desired number of fibers by referring to the required outlet air temperature shown in Fig. 16 or based on the required sensible and latent effectiveness indicated in Table 7, without having to repeat the iterative simulations. For instance, as shown in Fig. 16 (C), with inlet air temperature at 40°C, approximately 1750 and 2380 fibers would be required to achieve the outlet air temperature of 30°C, respectively, for $\dot{m}_{sol}/\dot{m}_{air}=10$ and $\dot{m}_{sol}/\dot{m}_{air}=5$. At $\dot{m}_{sol}/\dot{m}_{air}=10$, the dehumidifier with 1750 fibers will provide a total fiber surface area of 5.28m². This can be achieved by inserting those fibers into a cylindrical module with the module cross section diameter equal to 0.28m. As the incoming air mass flow rate doubles ($\dot{m}_{sol}/\dot{m}_{air}=5$), in order to achieve the same outlet temperature of 30°C, the required cylindrical module cross section diameter should be increased to 0.36 m. This means that larger fiber surface area will be required at higher inlet air mass flow rate. Similarly, by making use of Table 7, based on the required sensible and latent effectiveness for different operational conditions, the designer could easily select the relevant $\dot{m}_{sol}/\dot{m}_{air}$ and fibers number.

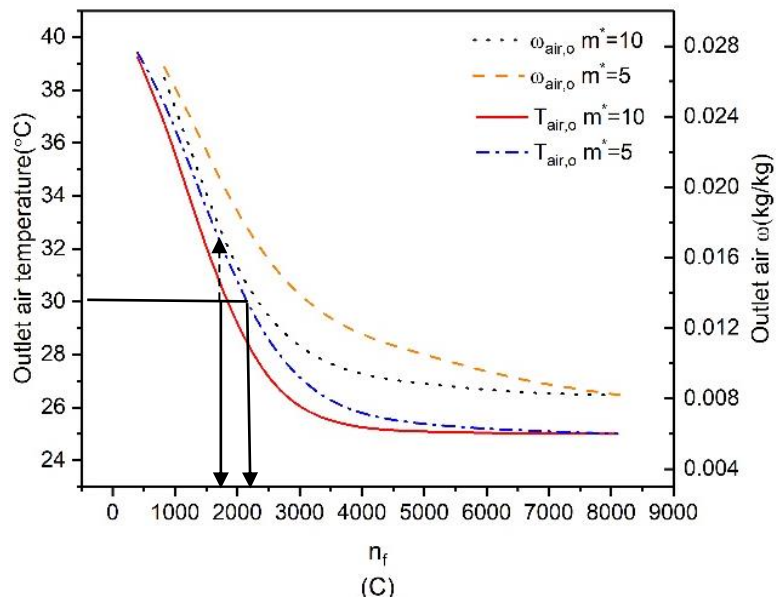
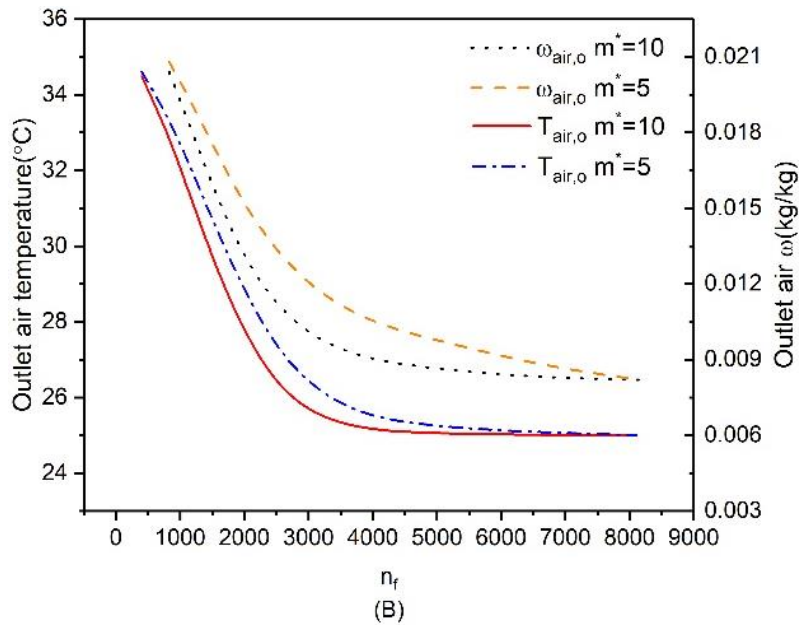
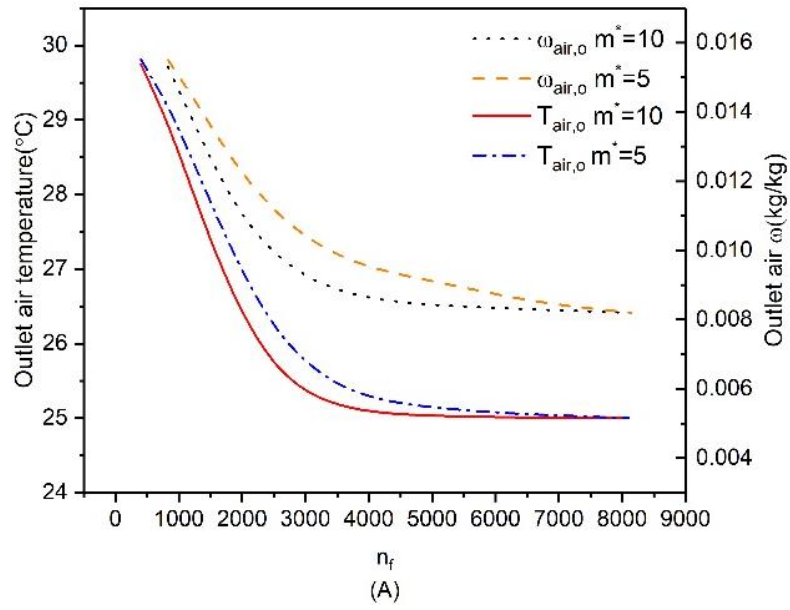


Fig. 16 The variations of outlet air temperature and specific humidity under various fiber numbers with $\dot{m}_{sol}/\dot{m}_{air}=10$ and $\dot{m}_{sol}/\dot{m}_{air}=5$ and inlet air temperature of (A) $T_{air,i}=30^{\circ}\text{C}$ (B) $T_{air,i}=35^{\circ}\text{C}$ (C) $T_{air,i}=40^{\circ}\text{C}$

Table 7 Variations of sensible effectiveness, latent effectiveness and outlet air conditions under various fiber numbers and $\dot{m}_{sol}/\dot{m}_{air}$ ratio ($T_{air,i}=35^{\circ}\text{C}$, $\omega_{air,i}=0.0215\text{kg/kg}$, $T_{sol,i}=25^{\circ}\text{C}$)

Number of fibers in the module	Inlet air mass flow rate	Mass flow rate ratio between inlet solution and inlet air	Outlet air conditions and associated effectiveness				
n_f	$\dot{m}_{air}(\text{kg/s})$	$\dot{m}_{sol}/\dot{m}_{air}$	$T_{air,o}(^{\circ}\text{C})$	$T_{sol,o}(^{\circ}\text{C})$	$\omega_{air,o}(\text{kg/kg})$	ϵ_{sen}	ϵ_{lat}
400	0.0087	10	34.49	25.30	0.0204	0.051	0.083
	0.0174	5	34.61	25.40	0.0208	0.039	0.053
	0.087	1	34.80	27.62	0.0213	0.020	0.015
	0.174	0.5	34.85	26.06	0.0214	0.015	0.008
900	0.0087	10	32.65	25.74	0.0172	0.235	0.323
	0.0174	5	33.19	26.09	0.0186	0.181	0.218
	0.087	1	34.10	30.07	0.0205	0.090	0.075
	0.174	0.5	34.36	28.10	0.0209	0.064	0.045
1600	0.0087	10	29.08	26.13	0.0129	0.592	0.647
	0.0174	5	30.24	26.81	0.0151	0.476	0.481
	0.087	1	32.60	31.32	0.019	0.240	0.188
	0.174	0.5	33.38	30.68	0.02	0.162	0.113
2500	0.0087	10	26.02	26.32	0.0101	0.898	0.857
	0.0174	5	27.03	27.26	0.0122	0.797	0.699
	0.087	1	30.41	31.83	0.0174	0.459	0.308
	0.174	0.5	31.90	32.73	0.0189	0.310	0.195
3600	0.0087	10	25.16	26.39	0.009	0.984	0.940
	0.0174	5	25.56	27.45	0.0122	0.944	0.827
	0.087	1	28.19	32.07	0.016	0.681	0.414
	0.174	0.5	30.05	33.86	0.018	0.495	0.263
4900	0.0087	10	25.05	26.42	0.0086	0.995	0.970
	0.0174	5	25.24	27.52	0.0097	0.976	0.887
	0.087	1	26.83	32.46	0.0149	0.817	0.496
	0.174	0.5	28.32	34.42	0.0172	0.668	0.323
6400	0.0087	10	25.01	26.49	0.0083	0.999	0.992
	0.0174	5	25.09	27.67	0.0088	0.991	0.955
	0.087	1	26.32	33.31	0.0132	0.868	0.624
	0.174	0.5	27.52	35.31	0.0157	0.748	0.436
8100	0.0087	10	25.00	26.56	0.0082	1.000	1.000
	0.0174	5	25.00	27.90	0.0082	1.000	1.000
	0.087	1	26.00	34.69	0.0103	0.900	0.842
	0.174	0.5	27.15	37.57	0.0121	0.785	0.707

6. Conclusions

This paper has reported a numerical model for a novel hollow fiber liquid desiccant dehumidification system. A thorough validation demonstrated that the modelled outlet parameters (temperature and specific humidity) for both the processed air and desiccant solution, and the heat and mass transfers under various testing situations were consistent with experimental results, analytical solutions, and results from the literature. Following its successful validation, the model was then used to predict the working performance of the dehumidifier. The effect of inlet parameters (inlet air velocity, inlet air specific humidity, inlet solution temperature, inlet solution concentration, inlet solution mass flow rate) and the air to solution specific humidity ratio on the sensible effectiveness, latent effectiveness and total effectiveness were parametrically assessed. The relationship between NTU and the sensible effectiveness, NTU_m and the latent effectiveness were also investigated. In addition, the temperature and humidity ratio contour for the air and solution were studied. The main conclusions of this paper can be summarized as follows:

(1) The effects of Cr^* and NTU, m^* and NTU_m on the sensible effectiveness and latent effectiveness are obvious. The sensible effectiveness has changed remarkably (from 0.35 to 1) with the increase of NTU in the range of 0.47 to 7 ($Cr^* = 0.13$). Meanwhile, the latent effectiveness has also changed remarkably with the increase of NTU_m in the range of 0 to 12, when m^* is 0.75.

(2) The increase in inlet air velocity will lead to the drop in sensible effectiveness, latent effectiveness, the inlet and outlet air temperature difference, and the inlet and outlet air relative humidity difference. As the incoming air velocity increases in the range of 1.5m/s to 4.5m/s, the sensible effectiveness drops from 0.74 to 0.08, and latent effectiveness decreases from 0.58 to 0.14. The sensible effectiveness is more sensitive to the solution inlet temperature, solution mass flow rate and solution concentration. The influences of the solution mass flow rate and the solution concentration on the latent effectiveness are less important in comparison with the sensible effectiveness.

(3) The moisture removal rate and air humidity ratio difference substantially grow with the increase of the ω_r^* . As the ω_r^* increases from 1.45 to 2.15, the sensible effectiveness decreases from 0.77 to 0.54, while the total effectiveness drops from 0.59 to 0.65. The changing ω_r^* has a very limited effect on the latent effectiveness.

(4) The increase of solution inlet temperature leads to a drop of sensible effectiveness, while the latent effectiveness remains more or less constant. For instance, as the solution inlet temperature rises from 20.5°C to 28.5°C, the sensible effectiveness declines from 0.37 to 0.17. Hence, a good way to achieve higher sensible effectiveness without affecting the latent effectiveness could be by decreasing the solution concentration.

(5) At 62% solution concentration, the latent effectiveness is about 0.47 when the inlet air velocity and solution mass flow rate is 0.087kg/s, which is comparable to the value obtained from the literature when LiCl was the desiccant[57]. Therefore, in order to achieve a similar dehumidification effect as in that case, a higher concentration of KCOOH desiccant solution should be used.

(6) The influence of fiber numbers on the dehumidification effectiveness, outlet air temperature and relative humidity have been analyzed and the results have been summarized in a user-

friendly table format. Without performing the iterative modelling, this Table can offer guidance to the designer for selecting the relevant solution to air mass flow ratio and fibers number, according to the required dehumidification effectiveness of the PHDF.

Acknowledgement

The authors greatly appreciate the financial contributions from the British funding body, Innovate UK (project code: 131821).

References

1. Artola, I., *Boosting Building Renovation: What Potential and Value for Europe? : Study*. 2016: European Parliament.
2. Isaac, M. and D.P. van Vuuren, *Modeling global residential sector energy demand for heating and air conditioning in the context of climate change*. Energy Policy, 2009. **37**(2): p. 507-521.
3. Hitchin, R., C. Pout, and P. Riviere, *Assessing the market for air conditioning systems in European buildings*. Energy and Buildings, 2013. **58**: p. 355-362.
4. Chua, K.J., et al., *Achieving better energy-efficient air conditioning – A review of technologies and strategies*. Applied Energy, 2013. **104**: p. 87-104.
5. Chen, X., et al., *Experimental investigations of polymer hollow fibre integrated evaporative cooling system with the fibre bundles in a spindle shape*. Energy and Buildings, 2017. **154**: p. 166-174.
6. Chen, X., et al., *A novel evaporative cooling system with a polymer hollow fibre spindle*. Applied Thermal Engineering, 2018. **132**: p. 665-675.

- 734 7. Peng, D. and X. Zhang, *An analytical model for coupled heat and mass transfer*
735 *processes in solar collector/regenerator using liquid desiccant*. Applied Energy, 2011.
736 **88**(7): p. 2436-2444.
- 737 8. Li, X., et al., *Dynamic modeling of a liquid desiccant dehumidifier*. Applied Energy, 2016.
738 **180**: p. 435-445.
- 739 9. Xiao, F., G. Ge, and X. Niu, *Control performance of a dedicated outdoor air system*
740 *adopting liquid desiccant dehumidification*. Applied Energy, 2011. **88**(1): p. 143-149.
- 741 10. Keniar, K., K. Ghali, and N. Ghaddar, *Study of solar regenerated membrane desiccant*
742 *system to control humidity and decrease energy consumption in office spaces*. Applied
743 Energy, 2015. **138**: p. 121-132.
- 744 11. Gao, W.Z., et al., *Experimental study on partially internally cooled dehumidification in*
745 *liquid desiccant air conditioning system*. Energy and Buildings, 2013. **61**: p. 202-209.
- 746 12. Yin, Y., et al., *Experimental study on a new internally cooled/heated*
747 *dehumidifier/regenerator of liquid desiccant systems*. International Journal of
748 Refrigeration, 2008. **31**(5): p. 857-866.
- 749 13. Luo, Y., et al., *Experimental study of internally cooled liquid desiccant dehumidification:*
750 *Application in Hong Kong and intensive analysis of influencing factors*. Building and
751 Environment, 2015. **93**: p. 210-220.
- 752 14. Bansal, P., S. Jain, and C. Moon, *Performance comparison of an adiabatic and an*
753 *internally cooled structured packed-bed dehumidifier*. Applied Thermal Engineering,
754 2011. **31**(1): p. 14-19.

- 755 15. Song, X., L. Zhang, and X. Zhang, *NTUm-based optimization of heat or heat pump*
756 *driven liquid desiccant dehumidification systems regenerated by fresh air or return air.*
757 Energy, 2018. **158**: p. 269-280.
- 758 16. Wang, X., et al., *A hybrid dehumidifier model for real-time performance monitoring,*
759 *control and optimization in liquid desiccant dehumidification system.* Applied Energy,
760 2013. **111**: p. 449-455.
- 761 17. Wu, Q., et al., *A regulation strategy of working concentration in the dehumidifier of*
762 *liquid desiccant air conditioner.* Applied Energy, 2017. **202**: p. 648-661.
- 763 18. Zhang, L., H. Wei, and X. Zhang, *Theoretical analysis of heat and mass transfer*
764 *characteristics of a counter-flow packing tower and liquid desiccant dehumidification*
765 *systems based on entransy theory.* Energy, 2017. **141**: p. 661-672.
- 766 19. Kumar, R., et al., *Multi absorber stand alone liquid desiccant air-conditioning systems*
767 *for higher performance.* Solar Energy, 2009. **83**(5): p. 761-772.
- 768 20. Das, R.S. and S. Jain, *Experimental performance of indirect air-liquid membrane*
769 *contactors for liquid desiccant cooling systems.* Energy, 2013. **57**: p. 319-325.
- 770 21. Bai, H., et al., *Influences of the mixed LiCl-CaCl₂ liquid desiccant solution on a*
771 *membrane-based dehumidification system: Parametric analysis and mixing ratio*
772 *selection.* Energy and Buildings, 2019. **183**: p. 592-606.
- 773 22. Xiong, Z.Q., Y.J. Dai, and R.Z. Wang, *Development of a novel two-stage liquid*
774 *desiccant dehumidification system assisted by CaCl₂ solution using exergy analysis*
775 *method.* Applied Energy, 2010. **87**(5): p. 1495-1504.

- 776 23. Luo, Y., et al., *Experimental and theoretical research of a fin-tube type internally-cooled*
777 *liquid desiccant dehumidifier*. Applied Energy, 2014. **133**: p. 127-134.
- 778 24. Luo, Y., et al., *Study on an internally-cooled liquid desiccant dehumidifier with CFD*
779 *model*. Applied Energy, 2017. **194**: p. 399-409.
- 780 25. Ou, X., et al., *Experimental investigations on heat and mass transfer performances of*
781 *a liquid desiccant cooling and dehumidification system*. Applied Energy, 2018. **220**: p.
782 164-175.
- 783 26. Das, R.S. and S. Jain, *Performance characteristics of cross-flow membrane contactors*
784 *for liquid desiccant systems*. Applied Energy, 2015. **141**: p. 1-11.
- 785 27. Ge, G., et al., *Comparison of experimental data and a model for heat and mass transfer*
786 *performance of a liquid-to-air membrane energy exchanger (LAMEE) when used for air*
787 *dehumidification and salt solution regeneration*. International Journal of Heat and Mass
788 Transfer, 2014. **68**: p. 119-131.
- 789 28. Ge, G., et al., *Analytical model based performance evaluation, sizing and coupling flow*
790 *optimization of liquid desiccant run-around membrane energy exchanger systems*.
791 Energy and Buildings, 2013. **62**: p. 248-257.
- 792 29. Moghaddam, D.G., et al., *Small-scale single-panel liquid-to-air membrane energy*
793 *exchanger (LAMEE) test facility development, commissioning and evaluating the*
794 *steady-state performance*. Energy and Buildings, 2013. **66**: p. 424-436.
- 795 30. Ge, G., et al., *Comparison of experimental data and a model for heat and mass transfer*
796 *performance of a liquid-to-air membrane energy exchanger (LAMEE) when used for air*

- 797 *dehumidification and salt solution regeneration*. International Journal of Heat & Mass
798 Transfer, 2014. **68**(1): p. 119-131.
- 799 31. Ghadiri Moghaddam, D., R.W. Besant, and C.J. Simonson, *Solution-side effectiveness*
800 *for a liquid-to-air membrane energy exchanger used as a dehumidifier/regenerator*.
801 Applied Energy, 2014. **113**: p. 872-882.
- 802 32. Ghadiri Moghaddam, D., R.W. Besant, and C.J. Simonson, *A methodology for scaling*
803 *a small-scale energy exchanger performance results to a full-scale energy exchanger*.
804 International Journal of Heat and Mass Transfer, 2015. **82**: p. 555-567.
- 805 33. Namvar, R., et al., *Transient heat and moisture transfer characteristics of a liquid-to-air*
806 *membrane energy exchanger (LAMEE) model verification and extrapolation*.
807 International Journal of Heat and Mass Transfer, 2013. **66**: p. 757-771.
- 808 34. Moghaddam, D.G., R.W. Besant, and C.J. Simonson, *Solution-side effectiveness for a*
809 *liquid-to-air membrane energy exchanger used as a dehumidifier/regenerator*. Applied
810 Energy, 2014. **113**(6): p. 872-882.
- 811 35. Chen, X., et al., *Recent research developments in polymer heat exchangers – A review*.
812 Renewable and Sustainable Energy Reviews, 2016. **60**: p. 1367-1386.
- 813 36. Zhang, L.-Z., et al., *Conjugate heat and mass transfer in a hollow fiber membrane*
814 *module for liquid desiccant air dehumidification: A free surface model approach*.
815 International Journal of Heat and Mass Transfer, 2012. **55**(13–14): p. 3789-3799.
- 816 37. Huang, S.M., et al., *Fluid flow and heat mass transfer in membrane parallel-plates*
817 *channels used for liquid desiccant air dehumidification*. International Journal of Heat &
818 Mass Transfer, 2012. **55**(9-10): p. 2571-2580.

- 819 38. Li, Z.X. and L.Z. Zhang, *Flow maldistribution and performance deteriorations in a*
820 *counter flow hollow fiber membrane module for air humidification/dehumidification.*
821 *Journal of Membrane Science*, 2014. **74**(1): p. 421-430.
- 822 39. Zhang, N., S.-Y. Yin, and L.-Z. Zhang, *Performance study of a heat pump driven and*
823 *hollow fiber membrane-based two-stage liquid desiccant air dehumidification system.*
824 *Applied Energy*, 2016. **179**: p. 727-737.
- 825 40. Zhang, N., S.-Y. Yin, and M. Li, *Model-based optimization for a heat pump driven and*
826 *hollow fiber membrane hybrid two-stage liquid desiccant air dehumidification system.*
827 *Applied Energy*, 2018. **228**: p. 12-20.
- 828 41. Liang, C.-H., L.-Z. Zhang, and L.-X. Pei, *Performance analysis of a direct expansion*
829 *air dehumidification system combined with membrane-based total heat recovery.*
830 *Energy*, 2010. **35**(9): p. 3891-3901.
- 831 42. Chen, X., et al., *Experimental investigations of polymer hollow fibre heat exchangers*
832 *for building heat recovery application.* *Energy and Buildings*, 2016. **125**: p. 99-108.
- 833 43. Riffat, S.B., S.E. James, and C.W. Wong, *Experimental analysis of the absorption and*
834 *desorption rates of HCOOK/H₂O and LiBr/H₂O.* *International Journal of Energy*
835 *Research*, 1998. **22**(12): p. 1099-1103.
- 836 44. Chen, X., et al., *Experimental investigation of a polymer hollow fibre integrated liquid*
837 *desiccant dehumidification system with aqueous potassium formate solution.* *Applied*
838 *Thermal Engineering*, 2018. **142**: p. 632-643.
- 839 45. Karlsson, H.O.E. and G. Trägårdh, *Heat transfer in pervaporation.* *Journal of*
840 *Membrane Science*, 1996. **119**(2): p. 295-306.

- 841 46. Zhang, L.Z., Y. Jiang, and Y.P. Zhang, *Membrane-based humidity pump: performance*
842 *and limitations*. Journal of Membrane Science, 2000. **171**(2): p. 207-216.
- 843 47. Zhang, L.Z., *Heat and mass transfer in a randomly packed hollow fiber membrane*
844 *module: A fractal model approach*. International Journal of Heat & Mass Transfer, 2011.
845 **54**(13): p. 2921-2931.
- 846 48. Zhang, L.Z., *Fabrication of a lithium chloride solution based composite supported liquid*
847 *membrane and its moisture permeation analysis*. Journal of Membrane Science, 2006.
848 **276**(1): p. 91-100.
- 849 49. Incropera, F.P. and D.P. DeWitt, *Fundamentals of heat and mass transfer, 6th Edition*.
850 Wiley, New York, 2006.
- 851 50. Seyed-Ahmadi, M., et al., *Transient behavior of run-around heat and moisture*
852 *exchanger system. Part I: Model formulation and verification*. International Journal of
853 Heat & Mass Transfer, 2009. **52**(25): p. 6000-6011.
- 854 51. Vali, A., et al., *Numerical model and effectiveness correlations for a run-around heat*
855 *recovery system with combined counter and cross flow exchangers*. International
856 Journal of Heat & Mass Transfer, 2009. **52**(25): p. 5827-5840.
- 857 52. Fumo, N. and D.Y. Goswami, *Study of an aqueous lithium chloride desiccant system:*
858 *air dehumidification and desiccant regeneration*. Solar Energy, 2015. **72**(4): p. 351-361.
- 859 53. Melinder, Å., *Thermophysical Properties of Aqueous Solutions Used as Secondary*
860 *Working Fluids Doctoral Thesis By*. Energiteknik, 2007.
- 861 54. Taylor, J.R., *Error Analysis The Study of Uncertainties in Physical Measurements 2nd*
862 *Edition*. Epfl, 1982.

- 863 55. Zhang, L.Z. and J.L. Niu, *Effectiveness Correlations for Heat and Moisture Transfer*
864 *Processes in an Enthalpy Exchanger With Membrane Cores*. Journal of Heat Transfer,
865 2002. **124**(5): p. 922-929.
- 866 56. RK;, S. and S. DP, *Fundamental of Heat Exchanger Design*. John Wiley & Sons,
867 Hoboken, NJ, 2003: p. 97-164.
- 868 57. Zhang, L.Z., *An Analytical Solution to Heat and Mass Transfer in Hollow Fiber*
869 *Membrane Contactors for Liquid Desiccant Air Dehumidification*. Journal of Heat
870 Transfer, 2011. **133**(9): p. 092001.

871

872 **Nomenclature**

A	hollow fiber surface area (m^2)
c_p	specific heat capacity (J/kgK)
Cr^*	heat capacity ratio
d	diameter (m)
d_h	hydrodynamic diameter (m)
h	convective heat transfer coefficient ($\text{W/m}^2\text{K}$)
h_{fg}	condensation heat of water (J/kg)
k	mass transfer coefficient (m/s)
L	length of the dehumidifier (m)
M	moisture removal rate (kg/s)
m^*	solution-to-air-mass flow rate ratio
\dot{m}	mass flow rate (kg/s)
m_{sen}	sensible heat capacity ratio
m_{lat}	latent heat capacity ratio
n	number of fibres inside the module
NTU	number of heat transfer units
NTU_m	number of mass transfer units
Nu	Nusselt number
Sh	Sherwood number
Sc	Schmidt number
P_{sol}	equilibrium vapour pressure of desiccant solution (Pa)
P	pressure (Pa)
Pr	Prandtl number
Re	Reynolds number
RH	relative humidity (%)
T	temperature ($^{\circ}\text{C}$)
u	velocity (m/s)
X	desiccant solution mass fraction ($\text{kg KCOOH/kg solution}$)

Greek symbols

λ	thermal conductivity (W/mK)
ω	specific humidity of the air (kg moisture/ kg air)
ω_r	air to solution specific humidity ratio
ϕ	packing fraction
μ	dynamic viscosity (Pa •s)
ε	effectiveness
δ	thickness of hollow fiber (m)
ρ	solution density (kg/m ³)
ν	kinematic viscosity (m ² /s)
τ	fractal dimension of the fiber module
ψ	diffusivity (m ² /s)

Subscripts

<i>air</i>	air flow
<i>atm</i>	atmospheric pressure
<i>c</i>	dehumidifier cross section
<i>crit</i>	critical value
<i>b</i>	bulk
<i>desi</i>	desiccant
<i>eq</i>	equivalent
<i>exp</i>	experimental
<i>f</i>	fiber
<i>h</i>	Hydraulic
<i>i</i>	inlet, inside
<i>lat</i>	latent
<i>lim</i>	limiting value
<i>m</i>	mass transfer/hollow fiber
<i>num</i>	numerical
<i>o</i>	outlet, outside
<i>ov</i>	overall
<i>s</i>	surface
<i>sen</i>	sensible
<i>sol</i>	solution flow
<i>tot</i>	total
<i>w</i>	water

873

874

875